SIAM J. APPL. MATH.
Vol. 66, No. 5, pp. 1533–1562

A SEMIANALYTICAL THERMAL STRESS MODEL FOR THE CZOCHRALSKI GROWTH OF TYPE III-V COMPOUNDS*

C. SEAN BOHUN†, IAN FRIGAARD‡, HUAXIONG HUANG§, AND SHUQING LIANG§

Abstract. In this paper we describe a semianalytical approach to computing the temperature and thermal stress inside a III-V compound grown with the Czochralski technique. An analysis of the growing conditions indicates that the crystal growth occurs on the conductive time scale. A perturbation method for the temperature field is developed for an arbitrary crystal profile using the Biot number as a (small) expansion parameter. The zeroth order solution is one-dimensional in the axial direction. Explicit solutions are obtained for a cylindrical and a conical crystal. Under typical growth conditions, a parabolic temperature profile in the radial direction is shown to arise naturally as the first order correction. As a result, the thermal stress is obtained explicitly and its magnitude is shown to depend on the zeroth order temperature and Biot number. Both the axial temperature gradient and crystal profile are shown to be important for controlling thermal stress and defect density. Some issues relevant to growth conditions are also discussed.

Key words. crystal growth, asymptotic expansion, moving interface, thermal stress, dislocation density, finite difference method, Czochralski technique

AMS subject classifications. 74A10, 74F05, 74H10, 80A22, 82D25, 82D37, 65M06

DOI. 10.1137/S0036139903436455

1. Introduction.

Directional solidification methods are widely used for growing large industrial sized crystals. Among them, the Czochralski (Cz) method is the most popular technique for growing crystals used by the semiconductor and related industries. By dipping a small seed crystal into a pool of molten material in the crucible and carefully controlling the heat balance inside the grower, a large crystal can be grown by pulling the crystal away from the melt in a slow and steady fashion. The pulling rod and the crucible are normally rotated in opposite directions during the growth period. Delicate control is often needed to maintain the crystal quality, and a slight change of the growth conditions may result in defect formation inside the crystal. With care, a single crystal with low defect density can be obtained routinely when the size of the crystal does not exceed a critical value. For a more detailed account of the Cz and other techniques, we refer the readers to the extremely informative handbooks by Hurle [16, 17].

Due to the complex nature of the thermal, structural, and dynamic coupling of the molten material, the crystal, the crucible, the gas chamber, and other parts of the grower, considerable efforts have been devoted to laboratory experiments and to modeling and simulation of the growth environment over the past several decades. As a result, there exists an extensive literature, mostly in engineering fields. These studies

*Received by the editors October 23, 2003; accepted for publication (in revised form) March 15, 2006; published electronically May 26, 2006. This work was supported by Firebird Semiconductors Ltd., the Mathematics of Information Technology and Complex Systems (MITACS), a Network of Centers of Excellence and the Nature Sciences and Engineering Research Council (NSERC) of Canada, and BCASI.

http://www.siam.org/journals/siap/66-5/43645.html

†Department of Mathematics, Pennsylvania State University, Mont Alto, PA 17237 (csb15@psu.edu).

‡Department of Mathematics, University of British Columbia, Vancouver V6T 1Z2, BC, Canada (frigaard@math.ubc.ca).

§Department of Mathematics and Statistics, York University, Toronto M3J 1P3, ON, Canada (hhuang@yorku.ca, sqliang@mathstat.yorku.ca).

cover a wide spectrum of areas, from decoupled one- or two-dimensional simulations to fully coupled three-dimensional computations; see, e.g., [4, 5, 16, 17, 18, 26, 27, 29]. Most of the studies rely heavily on computer simulation since the fully coupled system cannot be solved otherwise. These investigations have generated useful information including temperature distribution, crystal-melt interface shape, and melt flow patterns inside the crucible. By comparison, much less attention has been paid to the coupling of defect modeling and field variables even though significant progress has been made in identifying main factors that determine the formation of defects [31].

In this paper, we present a semianalytical approach for studying the temperature field inside the crystal and the related thermal stress. It is believed that defect formation can be related to an excessive thermal stress above some critical value; see, e.g., [1, 11, 13, 19, 29, 33, 34] and the references therein. Therefore, analysis of the growth factors that determine the stress level will be extremely useful for crystal growers. The stress analysis requires that a particular crystal structure be specified, and we have chosen the ZnS structure shared by the type III-V binary semiconductors. Even though the basic mathematical structure remains the same for any III-V compound, we will focus on indium antimonide (InSb) for the rest of the paper. InSb has the narrowest bandgap and highest temperature mobility of the III-V binary compound semiconductors. Because of these properties, InSb is widely used in both magnetic field detectors and infrared sensors. A review of these properties can be found in Micklethwaite and Johnson [24].

The primary reason for focusing on InSb is that it is exceedingly difficult to grow with the Cz technique mainly because of its small critically resolved shear stress (CRSS). It is known experimentally that attempting to grow InSb in a cylindrical profile with the Cz technique produces crystals with an unacceptable defect density, contrary to the growth of more common crystals such as silicon, where low defect density crystals can be grown in a cylindrical shape. Thus it is often an art to find the most suitable profile of the solidifying crystal by carefully varying the furnace temperature and the rate that the crystal is extracted [23]. To determine the influence of various resulting crystal profiles (i.e., axial variations of the lateral surface or crystal shapes) on the stress experienced within the crystal, we assume that the profile of the crystal is an arbitrary function of the axial displacement while allowing the solid-liquid interface to be driven by a Stefan condition and a compatibility condition at the solid-liquid-gas triple point.

By examining the physical process and parameter values of the growth environment closely, we are able to identify the main features associated with InSb crystals. In particular, if the heat flux from the melt is uniform across the crystal-melt interface, the temperature field will be dominated by the lateral flux through the crystal-gas surface, characterized by a nondimensional Biot number. The value of the Biot number is small under the growth conditions for InSb crystals, suggesting an asymptotic expansion of the solution in terms of this parameter. Much of the asymptotic framework discussed in this paper has appeared elsewhere in the literature [3, 14, 20, 35, 36, 37, 38, 39]. For example, Kuiken and Roksnoer [20] assumed a pseudosteady solid-liquid interface to obtain an accurate temperature distribution of a Si crystal grown with the floating-zone technique. Their solution takes the form of an expansion in terms of the Peclet and Nusselt numbers of the crystal, giving a solution valid for slender crystals grown in conductive heat transfer environments. By specifying an externally defined solid-liquid interface shape these authors avoided using a Stefan condition to evolve the interface. An asymptotic analysis that con-

sidered the melt was undertaken by Brattkus and Davis [3], where the geometry allowed an expansion in terms of the aspect ratio of the solidification cell. Young and Chait [36] considered a system driven by surface tension and more recently Young and Heminger [37, 38] have utilized a small aspect ratio to study the growth of single crystal fibers.

This paper blends the asymptotic expansion with the plane strain approximation to examine thermal stress inside the crystals. It contrasts significantly with the above references by assuming a radially independent heat flux from the melt that avoids a boundary layer analysis around the solidification front, greatly simplifying the asymptotics. Any angular dependence is minimized by the rotation of the seed and crucible, and the experimental evidence of an almost flat interface for Cz grown InSb crystals [23] suggests that the flux from the melt is likely to be largely independent of the radius. This is also supported in the literature [8, 9]. On the other hand, if the heat flux is radially dependent then the same asymptotic framework applies, but there will be a boundary layer solution similar to that in [3, 36] or [20] on the crystal side to match the asymptotic solutions.

While the details of the motion of the melt are ignored, the crystal-melt and crucible-melt heat transfer coefficients are estimated from the Ekman layer and natural convection submodel, respectively. As the crystal grows two situations are investigated. In the first, the flux is constant so that the model is more accurately a description of the solid in a directional solidification technique. In the second, the flux is calculated through an essentially zero-dimensional model for the melt. This enables the heat flux from the melt to be influenced by some of the crucible and operating parameters of the Cz process.

In the fully unsteady case, the asymptotic expansion results in a system of one-dimensional equations and the thermal stress can be obtained explicitly in an analytical form, under the plane strain assumption. In the pseudosteady limit this reduces to the classical result that the stress is proportional to the concavity of the temperature field [22, 34]. This also extends the work of [19], where stress was obtained for a cylindrical crystal with a flat crystal-melt interface. The pseudosteady solutions are contrasted with the unsteady solutions for cylindrical and conical crystals justifying the pseudosteady approximation for the growth parameters of InSb used in this paper. A detailed description of the pseudosteady approximation with respect to Cz growth can be found in the paper by Derby and Brown [10]. Other examples of the use of the pseudosteady approximation can be found elsewhere [14, 35].

Compared to most of the previous work using asymptotic or numerical methods, this study moves a step further by coupling stress calculation with the asymptotic field temperature solution and deriving an explicit form for the stress. Furthermore, formulated in a nondimensional form, the dependence of the stress level on the Biot number is useful for crystal growers when larger crystals are grown. Since the Biot number is proportional to the product of the heat transfer coefficient and the mean crystal radius, it is obvious that one should try to reduce the heat flux via the lateral surface when a crystal of larger radius is grown. In addition, the explicit nature of the stress solution enables us to identify the effect of crystal profile (shape) as well as the crystal size (radius) on the stress. More importantly, obtaining an explicit formulation for the stress allows us to apply other techniques such as optimal control methodologies to efficiently search for better growth conditions. A simplified model for the heat exchange between the gas flow and the crystal is used to clarify the presentation. However, the asymptotic solution developed here is still valid if a more

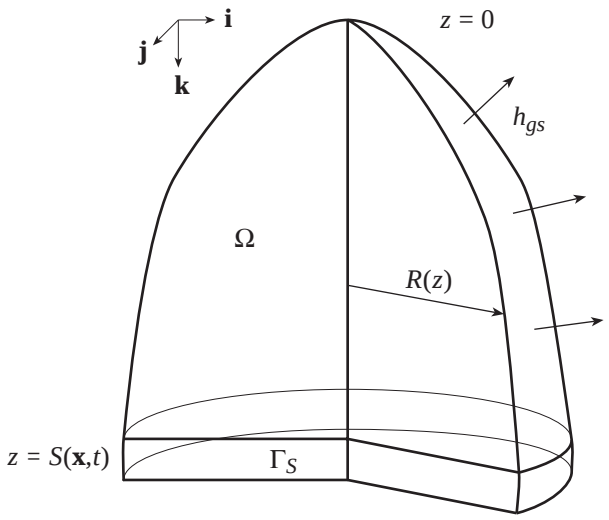

FIG. 1. *Shown is a typical crystal at some time t during a growth run with a newly solidified portion at* $z = S(\mathbf{x}, t)$. *The coordinate system is chosen so that the top of the crystal remains at* $z = 0$ *and the solidification front grows downward in the positive z direction. The radial profile is given by* $R(z)$ *and the crystal length is* $S(\mathbf{x}, t)$. *Finally, the heat transfer coefficient* h_{gs} *may be a function of the axial position z.*

realistic model for the gas is incorporated. More detailed discussion related to the growth conditions for InSb will be given in sections 2 and 5.

The rest of the paper is organized as follows. In section 2, we will present the mathematical model and dimensional analysis. Asymptotic solutions are given in section 3. Thermal stress is discussed in section 4. In section 5, results are presented for both pseudosteady and unsteady cases. We conclude the paper with a brief summary and discussion on future directions in section 6.

2. Mathematical model and dimensional analysis. The basic assumptions made in this study are (1) the crystal is axis-symmetric; (2) the heat exchange between the crystal and gas along the lateral surface of the crystal is a constant; (3) the heat exchange between the crystal and melt along the crystal-melt interface is uniform; (4) the mean crystal radius is small compared to its length; (5) thermal stress is elastic and computed under a plane strain assumption. Some of the assumptions are made to simplify the derivation, and others are made based on previous study of similar problems or observations made by us and engineers we have been collaborating with. We will revisit some of the assumptions in section 6.

Figure 1 illustrates the geometry of a typical crystal. The coordinate system is fixed to the top of the growing crystal at $z = 0$, the final length of the crystal is denoted Z, and the crystal radius is denoted $R(z)$. The growth starts with a seed crystal with radius of order $R_0 = 0.5$ cm and length $Z_0 = 3$ cm. The crystal grows outward in a slowly developing cone, eventually reaching a radius $R(Z) \simeq 5$ cm after a length $Z \simeq 30$ cm. A crystal can take 10–20 hours to grow. Thus, at the outset we make two observations. First, the crystal growth is characterized by a large aspect ratio. Second, it is evident that any transients in the system, unless caused by rapidly changing boundary conditions, are very slow. These two features will be used to derive our eventual model.

Within the crystal Ω, the temperature $T(\mathbf{x}, t)$ satisfies the heat equation

$$\rho_s c_s \frac{\partial T}{\partial t} = k_s \sum_j \frac{\partial^2 T}{\partial x_j^2}, \qquad \mathbf{x} \in \Omega,\ t > 0, \tag{1}$$

where ρ_s, c_s, and k_s, respectively, are the density, specific heat, and thermal conductivity of the crystal solid phase. The lateral surface of the crystal is denoted Γ_g and is subjected to cooling from the circulating chamber gases and from radiative heat losses. Although radiation is not insignificant, for simplicity we model both effects through a simple Newtonian cooling law

$$-k_s \frac{\partial T}{\partial \mathbf{n}} = h_{gs}(T - T_g), \qquad \mathbf{x} \in \Gamma_g. \tag{2}$$

Here we assume that the heat transfer coefficient h_{gs} incorporates both convective and radiative heat transfer (the latter via linearization). The top of the crystal is fixed at $z = 0$, where we also invoke a Newtonian cooling law

$$k_s \frac{\partial T}{\partial z} = h_{ch}(T - T_{ch}), \tag{3}$$

in the case that the radius at $z = 0$ is assumed to be nonzero. Here h_{ch} represents the heat transfer coefficient for the seed-chuck connection and T_{ch} is the chuck temperature.

The crystal-melt interface is denoted Γ_S and is where $T = T_m$, the melting temperature. The interface of the phase transition is thus implicitly defined from the temperature field. Explicitly we denote the melting isotherm by

$$z - S(\mathbf{x}, t) = 0, \qquad \mathbf{x} \in \Gamma_S. \tag{4}$$

The motion of the interface of the phase transition is governed by the Stefan condition

$$\rho_s L\, |\vec{v}_n| = k_s \left.\frac{\partial T}{\partial \mathbf{n}}\right|_{z \to S^-} - q_{l,n}, \tag{5}$$

where $|\vec{v}_n|$ is the speed at which the interface moves in the direction of the outward unit normal $\mathbf{n}$, L is the latent heat, and $q_{l,n}$ is the heat flux from the melt normal to the interface.

Figure 2 illustrates the triple point (TP) where the solid, liquid, and gas come into contact and the solid-liquid interface moves at a velocity $\vec{v}_n = v_n \mathbf{n}$. If $\partial S/\partial t$ denotes the speed of the interface in the $\mathbf{k}$ direction, then

$$|\vec{v}_n| = v_n = \frac{\partial S}{\partial t} \mathbf{k} \circ \mathbf{n}. \tag{6}$$

Still referring to Figure 2, the profile (shape) of the crystal $R(z)$ is determined by the motion of the TP given by

$$\left.\frac{\partial R}{\partial t}\right|_{z=S} = \tan(\theta - \theta_c) \left.\frac{\partial S}{\partial t}\right|_{r=R}, \tag{7}$$

where θ_c is the contact angle formed by the wetting fluid (melt) and the crystal and θ is the angle formed by the meniscus with the vertical z-axis. This expression simply

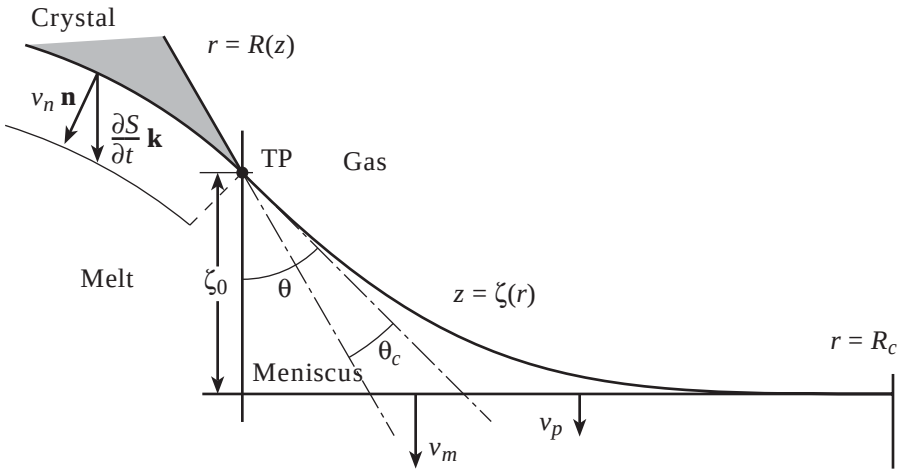

FIG. 2. *Schematic diagram of the meniscus $z = \zeta(r)$ with capillary height ζ_0, defined on $R(S) \le r \le R_c$, where $R(S)$ is the radius of the crystal at the interface, θ_c is the contact angle, and R_c is the radius of the crucible. The motion of the TP is determined by the advancing interface S, the speed at which the melt falls v_m, and the pull rate applied to the crucible v_p.*

states that the crystal prefers to grow in the direction defined by the contact angle. The motion of the advancing interface S, the advancement due to the pulling rate, and the motion due to the loss of melt determine the vertical position of the triple junction ζ_0 via

$$\frac{d\zeta_0}{dt} = v_p + v_m - \frac{\partial S}{\partial t}, \tag{8}$$

where v_m is the rate at which the melt-gas surface drops given by

$$v_m = \frac{\rho_s R^2}{\rho_l R_c^2} \frac{\partial S}{\partial t} \tag{9}$$

from the law of mass conservation and v_p is the pulling rate at which the crucible is dropped to ensure that the crystal-melt interface remains at the surface of the liquid.

We note that properly it is necessary to close the model by relating growth in S to that in R, i.e., solving (7). To do this we must model the crystal withdrawal from the crucible, the formation of the meniscus, and the coupling of S and R. It has been shown in [32] that the growth angle is related to the capillary height ζ_0 for large Bond number growth. In principle, crystals with desirable shapes can be grown by adjusting the pulling rate, which determines the meniscus angle θ in (7). Therefore, if we are not interested in the dynamics, we can impose a geometry $R(z)$ on the model. This approach has the advantage of allowing us to investigate the thermal fields and associated stresses that develop for a particular observed shape.

Note that for cylindrical crystals the capillary height does not change throughout the growth cycle. Therefore (8) can be simplified as

$$v_p = \frac{\partial S}{\partial t} - v_m. \tag{10}$$

TABLE 1
A summary of the thermophysical and typical growth parameters of InSb.

Data	Symbol	Value
Growing properties		
Mean crystal radius	$\overline{R}$	0.03 m
Final crystal length	Z	0.30 m
Characteristic growth rate	$\overline{v}$	6.9×10^{-6} m/s
Ambient gas temperature	T_g	600 K
Solid properties at $T = T_m$		
Melting temperature	T_m	798.4 K
Density	ρ_s	5.64×10^3 kg/m^3
Thermal conductivity	k_s	4.57 W/m K
Heat capacity	$\rho_s c_s$	1.5×10^6 J/m^3 K
Latent heat of fusion	L	2.3×10^5 J/kg
Heat transfer coefficients		
Crystal-gas	h_{gs}	$1 - 4$ W/m^2 K

2.1. Typical scales in InSb crystal growth. Although it is possible to treat the three-dimensional case above, it is somewhat unwieldy, and hence we instead attempt to simplify the model first. Table 1 specifies a typical set of thermophysical and process data. Consider a time t, after any initial growth transient, when the crystal has length S onto which a thin layer of crystal of radius $\overline{R}$ has just solidified. Utilizing (1) and the characteristic values in Table 1, the conduction of heat across a crystal cross-section and the time taken to grow a length $\overline{R}$ of crystal have the following time scales:

$$t_{\text{cond}} \simeq \frac{\overline{R}^2 \rho_s c_s}{k_s} = 3.0 \times 10^2 \text{ s}, \qquad t_{\text{grow}} \simeq \frac{\overline{R}}{\overline{v}} = 1.7 \times 10^4 \text{ s}.$$

Thus, the conductive time scale is typically much shorter than that for growth (i.e., over similar length scales). The growth time scale for the entire crystal is still longer and given by $t \simeq Z/\overline{v}$. It is over this latter growth time scale that significant changes in either the radius or area occur related to significant changes in the cooling capacity and heat capacity, respectively.

Therefore, apart from imposed rapid changes in the growth (e.g., at the start of the process and at the end as the crystal is withdrawn from the melt), all other thermal changes are slow and occur on the growth time scale. Since there is no process change that occurs on the conductive time scale, the process is likely to be pseudosteady on the growth related time scale.

Turning now to the thermal gradients, the magnitude of the radial variation in the temperature is maximized at the lateral surface where the crystal comes into contact with the surrounding gas. From (2) and Table 1,

$$\left|\frac{\partial T}{\partial n}\right|_{\Gamma_g} \leq \frac{h_{gs}}{k_s}(T_m - T_g) \simeq 175 \text{ K/m}.$$

The magnitude of the axial temperature gradient is maximal at the interface of the phase transition where the Stefan condition (5)–(6) is satisfied. Assuming a nearly flat interface, which will be justified later, an estimate for $T_z|_{S^-}$ is obtained by neglecting the heat flux in the liquid phase

$$\left|\frac{\partial T}{\partial z}\right|_{S^-} \simeq \frac{\rho_s L \overline{v}}{k_s} = 850 \text{ K/m}.$$

The sides of the crystal are predominantly vertical and the crystal-melt interface predominantly horizontal. Thus, we see that the vertical gradients dominate, at least in some neighborhood of the crystal-melt interface. However, we must note that the vertical gradients arise mostly due to heat loss to the cooling gases, which occurs in the radial direction. Since the cooling influences are weak, this implies that a long crystal is needed to get a significant temperature drop along the crystal length and suggests we will need to scale the axial and radial directions differently.

2.2. Nondimensionalization. The above discussion motivates our scaling below. For simplicity, we start by assuming an axisymmetric model, although the crystal cross-section is not in fact circular. The other assumptions that we make here, for simplicity only, are that the heat transfer coefficient h_{gs} and the gas temperature T_g are constant. In reality there will be local variations along the crystal surface, but in any case these require a more detailed analysis of the gas flows in order to be properly evaluated.

We define the Biot number by

$$\epsilon = \frac{h_{gs}\overline{R}}{k_s}, \tag{11}$$

and using the parameter values in Table 1, we find $\epsilon \lesssim 0.026 \ll 1$. We seek an asymptotic expansion in terms of ϵ. With this in mind we adopt the following scalings:

$$r = \overline{R}\hat{r}, \qquad R(z) = \overline{R}\hat{R}(\hat{z}), \quad \epsilon^{1/2}z = \overline{R}\hat{z}, \qquad \epsilon^{1/2}S(r,t) = \overline{R}\hat{S}(\hat{r},\hat{t}),$$

$$\Delta T = T_m - T_g, \qquad \mathrm{St} = \frac{L}{c_s\Delta T}, \qquad T = T_g + \Delta T\Theta, \qquad t = \frac{\mathrm{St}\,\overline{R}^2\rho_s c_s}{k_s\epsilon}\hat{t}.$$

Here variables with hats ($\hat{}$) are the nondimensional ones. In terms of these variables the heat equation in the crystal (1) becomes

$$\frac{\epsilon}{\mathrm{St}}\Theta_t = \frac{1}{r}(r\Theta_r)_r + \epsilon\Theta_{zz}, \qquad \mathbf{x}\in\Omega,\ t>0, \tag{12a}$$

with boundary conditions (2)–(4) becoming

$$-\Theta_r + \epsilon\Theta_z R'(z) = \epsilon\left[1+\epsilon(R'(z))^2\right]^{1/2}\Theta, \qquad \mathbf{x}\in\Gamma_g, \tag{12b}$$

$$\Theta_z(0,t) = \delta(\Theta(0,t) - \Theta_{ch}), \tag{12c}$$

$$\Theta = 1, \qquad \mathbf{x}\in\Gamma_S, \tag{12d}$$

where $\delta = \epsilon^{1/2}h_{ch}/h_{gs}$. The hats have been dropped for brevity. The crystal-melt interface advances according to the Stefan condition (5)–(6) which in nondimensional coordinates becomes

$$\Theta_z - \frac{1}{\epsilon}S_r\Theta_r = (\gamma + S_t), \qquad \gamma = \frac{q_l\overline{R}}{\epsilon^{1/2}k_s\Delta T}, \tag{12e}$$

where q_l and γ are the dimensional and nondimensional heat fluxes in the liquid across the crystal-melt interface in the axial direction. Note that we have chosen the rate of solidification to define the characteristic time scale. The Stefan number St gives the ratio of this characteristic solidification time scale to the time scale associated with conductive heat loss through the crystal side surface. Based on the parameter values in Table 1, we have $\mathrm{St} \simeq 4.3$, suggesting that the conductive scale is small and the temperature inside the crystal is steady on the growth time scale.

2.3. Growth conditions. Under general growth conditions the process may be pseudosteady. However, near the end of the process, transient influences may become important. To investigate both possibilities two situations are considered.

1. The growth of the crystal is characterized by an externally chosen value of q_l (or the nondimensional flux γ), constant for the duration of the simulation.
2. Using the temperature of the crucible Θ_c as a control parameter, q_l is determined implicitly by an effective heat transfer coefficient of the crucible to the crystal through the melt.

In the second scenario a simple model is used to couple the heat fluxes inside the grower based on the fact that the system is almost at thermal equilibrium. The nondimensional liquid temperature satisfies

(13a)
$$\frac{\phi}{\lambda\,\mathrm{St}}\frac{d}{dt}\left[\left(\frac{T_g}{\Delta T}+\Theta_l\right)V_l\right]=-\mu\lambda^2\frac{h_{sl}}{h_{gs}}A(\Theta_l-1)-\mu\frac{h_{gl}}{h_{gs}}(A_c-\lambda^2A)\Theta_l+\frac{h_{cl}}{h_{gs}}A_l(\Theta_c-\Theta_l)$$

with $\Theta_l(0)=1$ and $\Theta_c(0)$ chosen so that $\Theta_l'(0)=0$. The detailed derivation is given in the appendix, and from expression (47c) the γ in (12e) becomes

(13b)
$$\gamma=\epsilon^{1/2}\frac{h_{sl}}{h_{gs}}(\Theta_l-1).$$

3. Perturbation solution. We now seek to approximate the scaled model in section 2.2 via a straightforward perturbation expansion. In turn, this perturbation model will form the basis for a numerical solution. Since St is O(1) under the current growth conditions it is retained as a parameter. Equations (12a) and (12b) strongly suggest that the temperature Θ is independent of r to leading order. If true, then the crystal-melt interface S is also independent of r to leading order, and we see that this is consistent in (12e) with the growth being driven primarily by the vertical gradients. These observations motivate the following approximations:

(14)
$$\begin{aligned}\Theta&\sim\Theta_0(z,t)+\epsilon\Theta_1(r,z,t)+\epsilon^2\Theta_2(r,z,t)+\cdots,\\ S&\sim S_0(t)+\epsilon S_1(r,t)+\epsilon^2S_2(r,t)+\cdots.\end{aligned}$$

We substitute them into the scaled model, expand in powers of ϵ, simplify, and collect terms. The resulting field equations to first order are

(15a)
$$\frac{1}{\mathrm{St}}\Theta_{0,t}-\Theta_{0,zz}=\frac{1}{r}\frac{\partial}{\partial r}(r\Theta_{1,r}),\qquad \mathbf{x}\in\Omega,\ t>0,$$

(15b)
$$\frac{1}{\mathrm{St}}\Theta_{1,t}-\Theta_{1,zz}=\frac{1}{r}\frac{\partial}{\partial r}(r\Theta_{2,r}),\qquad \mathbf{x}\in\Omega,\ t>0,$$

where the boundary condition on the lateral surface becomes

(16a)
$$(\Theta_{1,r}-R'\Theta_{0,z}+\Theta_0)(R(z),z,t)=0,$$

(16b)
$$\left(\Theta_{2,r}-R'\Theta_{1,z}+\frac{1}{2}R'^2\Theta_0+\Theta_1\right)(R(z),z,t)=0.$$

Continuing this procedure for the remaining conditions, at the top of the crystal one has

$$\begin{aligned}\Theta_{0,z}(0,t)&=\delta(\Theta_0(0,t)-\Theta_{ch}),\\ \Theta_{1,z}(r,0,t)&=\delta\Theta_1(r,0,t),\end{aligned}$$

and at the solid-liquid interface

$$\Theta_0(S_0(t),t) = 1, \tag{17a}$$

$$(S_1\Theta_{0,z} + \Theta_1)(r, S_0(t), t) = 0. \tag{17b}$$

Finally, the evolution of the interface is governed by

$$S_0'(t) = \Theta_{0,z}(S_0(t),t) - \gamma, \qquad S_0(0) = Z_0, \tag{18a}$$

$$S_{1,t}(r,t) = \left(\Theta_{1,z} + S_1\Theta_{0,zz} + \frac{\Theta_{1,r}^2}{\Theta_{0,z}}\right)(r, S_0(t), t), \qquad S_1(r,0) = 0, \tag{18b}$$

where we have used (17b) to eliminate the $S_{1,r}$ term. We note that by expanding the solid-liquid interface into the same asymptotic series and deriving the above equations, we have implied that the interface will adjust its shape to avoid a temperature singularity at the solid-liquid-gas triple point. We also note that Z_0 is the nondimensional length of the seed. In addition there will be symmetry conditions at $r = 0$ for Θ_k, S_k, $k = 0, 1$.

3.1. Resolution of the zeroth order model. Integrating (15a) once and imposing the symmetry condition $\Theta_{1,r} = 0$ at $r = 0$, we have

$$\frac{r}{2}\left(\frac{1}{\mathrm{St}}\Theta_{0,t} - \Theta_{0,zz}\right) = \Theta_{1,r}.$$

Applying (16a) at $r = R$ gives the zeroth order problem

$$\frac{1}{\mathrm{St}}\Theta_{0,t} - \Theta_{0,zz} = \frac{2}{R}\left(R'\Theta_{0,z} - \Theta_0\right), \qquad 0 < z < S_0(t),\ t > 0, \tag{19a}$$

$$\Theta_{0,z}(0,t) = \delta(\Theta_0(0,t) - \Theta_{ch}), \qquad t \geq 0, \tag{19b}$$

$$\Theta_0(S_0(t),t) = 1, \qquad t \geq 0, \tag{19c}$$

$$S_0'(t) = \Theta_{0,z}(S_0(t),t) - \gamma, \qquad S_0(0) = Z_0,\ t > 0, \tag{19d}$$

with an initial condition $\Theta_0(z,0) = f(z) \leq 1$ compatible with the boundary conditions. Provided that $R \in C^1([0, S_0])$, the Stefan problem will have a unique solution. For details see Friedman [12].

Equation (19a) is parabolic and involves only the heat fluxes along the length of the crystal. With the chosen expansion we see that at zeroth order the temperature field has no radial dependence. In addition, we can see that the thermal gradients, as discussed previously, are caused by cooling effects at the surface. In section 5.1 we solve the time dependent system (19) on $0 < z < S_0(t)$ for a suitable set of initial conditions. Also notice expression (19d) illustrates that the chosen time scale balances the growth. The appearance of $\mathrm{St} > 1$ in (19a) suggests that thermal transients in the bulk of the crystal are not as important as the growth transient. This is explored further in section 5.1. The limit as $\mathrm{St} \to \infty$ leads naturally to a pseudosteady leading order model in which time dependency enters the thermal model only through the growth; i.e., we also solve as the pseudosteady limit

$$\Theta_{0,zz} + \frac{2}{R}\left(R'\Theta_{0,z} - \Theta_0\right) = 0, \qquad 0 < z < S_0(t),\ t > 0, \tag{20}$$

with (19b)–(19d). Expression (20) together with (19b)–(19d) is analogous to a Hele–Shaw problem, and it is well known that in one dimension solutions of the Stefan

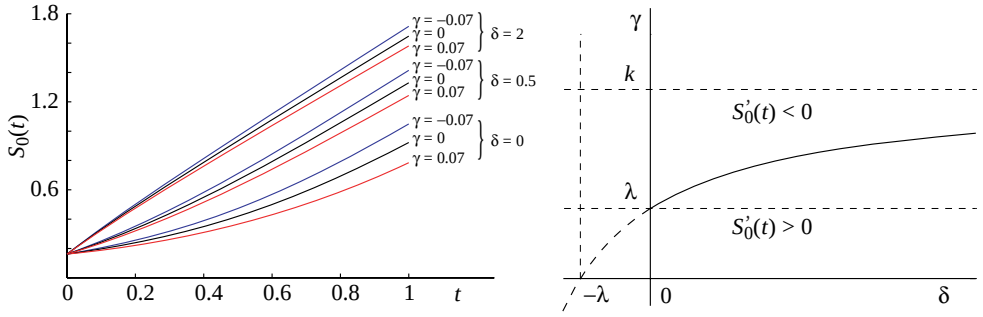

FIG. 3. *To the left is the evolution of the length of a cylindrical crystal grown using the pseudosteady approximation according to* (22). *For the simulations,* $\Theta_{ch} = 0$, $R_0 = 1$, $Z_0 = 0.162$ *(3 cm), and* $\epsilon = 0.026$ *(*$h_{gs} = 4\,W/m^2K$*). The position* $S_0 = 1.8$ *at* $t = 1$ *corresponds to a crystal length of 33 cm grown in 13.6 hours, typical for Cz grown InSb* [24]. *The curve on the right is* $S_0'(t) = 0$, *which characterizes the balance of the heat flux from the melt with the loss of heat at the chuck. The quantity* $\lambda = k \tanh kS_0$ *increases with* S_0.

problem (19) converge to solutions of Hele–Shaw as $\mathrm{St} \to \infty$. However, the convergence is not uniform and the intermediate asymptotic behaviors are different [30].

We start by exploring two special cases for which an analytic solution may be computed to the pseudosteady model.

3.1.1. Constant radius crystals. In this case we take $R(z) = R_0$, and (20) becomes simply

$$\Theta_{0,zz} - \frac{2}{R_0}\Theta_0 = 0, \qquad 0 < z < S_0(t),\ t > 0,$$

with boundary conditions (19b) and (19c). Solving for Θ_0 gives

$$\Theta_0(z,t) = \frac{k\cosh kz + \delta \sinh kz + \delta\Theta_{ch}\sinh k(S_0 - z)}{k\cosh kS_0 + \delta \sinh kS_0}, \quad k^2 = \frac{2}{R_0}. \tag{21}$$

The crystal grows at a rate governed by the Stefan condition (19d)

$$S_0'(t) = k\frac{k\sinh kS_0 + \delta\cosh kS_0 - \delta\Theta_{ch}}{k\cosh kS_0 + \delta\sinh kS_0} - \gamma, \quad S_0(0) = Z_0. \tag{22}$$

The left-hand side of Figure 3 shows the time dependence of the position of the interface and therefore the length of the crystal as a function of time for various combinations of δ and γ. The right-hand side details the balance between these two parameters. The initial position of the curve is determined by the length of the seed Z_0. If the γ, δ pair is chosen above the curve $S_0'(t) = 0$ $\big(\gamma > \gamma_{\max}(\delta) = k^2(\lambda_0 + \delta)/(k^2 + \delta\lambda_0), \lambda_0 = k\tanh kZ_0, \Theta_{ch} = 0\big)$, the seed melts back. If we are below the curve, then $S_0(t)$ increases without bound and the curve asymptotically approaches $\gamma = k$. For small S_0, (22) gives $S_0' = k^2S_0 - \gamma + \delta(1-\Theta_{ch})(1-\delta S_0) + \mathcal{O}(S_0^2)$ and for large S_0, the growth rate is asymptotically $S_0' = k - \gamma$.

3.1.2. Conical crystals. One source of ambiguity in the constant radius model above is the need to specify the chuck temperature and heat transfer coefficient. In the case of a conical crystal, which is closer to reality, this ambiguity is less prominent. We assume $R(z) = R_0 + \alpha z$, where $\arctan\alpha \simeq \mathcal{O}(1)$ is one-half the opening angle of

the crystal when using nondimensional units. This assumption is predicated on the condition that the dimensional version of $\alpha \simeq \mathcal{O}(\sqrt{\epsilon})$, and it is easily verified using the data in Table 1. Substituting for $R(z)$ we solve

$$\Theta_{0,\eta\eta} + \frac{2}{\eta}(\Theta_{0,\eta} - \Theta_0) = 0, \qquad R_0 < \alpha^2\eta < R_0 + \alpha S_0,\ t > 0, \tag{23a}$$

$$\Theta_{0,\eta} = \alpha\delta(\Theta_0 - \Theta_{ch}), \qquad \alpha^2\eta = R_0,\ t \geq 0, \tag{23b}$$

$$\Theta_0 = 1, \qquad \alpha^2\eta = R_0 + \alpha S_0,\ t \geq 0, \tag{23c}$$

where $\alpha^2\eta(z) = R_0 + \alpha z$. The resulting solution takes the form of linear combinations of modified Bessel functions

$$\Theta_0(\eta, t) = \frac{W_{fg}(\eta, \eta(0)) - \alpha\delta\left[V_{fg}(\eta, \eta(0)) - \Theta_{ch}V_{fg}(\eta, \eta(S_0))\right]}{W_{fg}(\eta(S_0), \eta(0)) - \alpha\delta V_{fg}(\eta(S_0), \eta(0))}, \tag{24}$$

where

$$W_{fg}(x,y) = \begin{vmatrix} f(x) & g(x) \\ f'(y) & g'(y) \end{vmatrix}, \quad V_{fg}(x,y) = \begin{vmatrix} f(x) & g(x) \\ f(y) & g(y) \end{vmatrix},$$
$$f(\eta) = \frac{I_1(\sqrt{8\eta})}{\sqrt{\eta}}, \qquad g(\eta) = \frac{K_1(\sqrt{8\eta})}{\sqrt{\eta}}.$$

The corresponding expression for the growth rate is

$$S_0'(t) = \frac{1}{\alpha}\frac{V_{f'g'}(\eta(S_0), \eta(0)) + \alpha\delta\left[W_{fg}(\eta, \eta(0)) - \Theta_{ch}W_{fg}(\eta, \eta(S_0))\right]}{W_{fg}(\eta(0), \eta(S_0)) - \alpha\delta W_{fg}(\eta(S_0), \eta(S_0))} - \gamma, \quad S_0(0) = Z_0.$$

Two limiting cases are considered. To compare with the cylindrical case one sets $R_0 = 1$ and expands (24) in a power series of α yielding

$$\Theta_0(z,t) = \frac{\cosh\sqrt{2}z}{\cosh\sqrt{2}S_0}\left\{1 - \frac{\alpha}{8}\left[6(z - S_0) + \sqrt{8}(z^2 - U)\tanh\sqrt{2}z \right.\right. \\ \left.\left. -\sqrt{8}(S_0^2 - U)\tanh\sqrt{2}S_0\right]\right\} + \mathcal{O}(\alpha^2) \tag{25a}$$

with

$$U = \frac{3}{2} + 2\delta\left(1 - \Theta_{ch}\cosh\sqrt{2}S_0\right). \tag{25b}$$

Expressions (25) should be compared to (21). Since for a cone $R_0 \ll 1$, a simple form of (24) can be obtained by expanding the solution in R_0 as

$$\Theta_0(z,t) = \sqrt{\frac{S_0}{z}}\frac{I_1(\sqrt{8z/\alpha})}{I_1(\sqrt{8S_0/\alpha})}\left[1 + \frac{R_0}{\alpha}\left(\sqrt{\frac{2}{\alpha z}}\frac{I_0(\sqrt{8z/\alpha})}{I_1(\sqrt{8z/\alpha})} \right.\right. \\ \left.\left. -\sqrt{\frac{2}{\alpha S_0}}\frac{I_0(\sqrt{8S_0/\alpha})}{I_1(\sqrt{8S_0/\alpha})} - \frac{1}{z} + \frac{1}{S_0}\right)\right] + \mathcal{O}(R_0^2). \tag{26}$$

The solution for conical crystals is more complicated, and we will defer the discussion to section 5.

3.1.3. Comments. This model for a one-dimensional temperature variation in the axial direction is not new. For example, it has been used in [32] but without formal justifications. What we have done here, by deriving it using asymptotic expansion, is to allow the reader to realize the applicability and restrictions of the model.

3.2. Radial variations: Resolution of the first order model. Having solved the zeroth order model, to give Θ_0 and S_0, we can resolve the radial variations in temperature, which occur at first order in Θ_1, and also consider the shape of the crystal-melt interface as it evolves, through S_1. From resolution of the zeroth order model we have

$$\Theta_{1,r} = \frac{r}{2}\left(\frac{1}{\mathrm{St}}\Theta_{0,t} - \Theta_{0,zz}\right),$$

and integrating with respect to r we have

$$\Theta_1(r,z,t) = \Theta_1(0,z,t) + \frac{r^2}{4}\left(\frac{1}{\mathrm{St}}\Theta_{0,t} - \Theta_{0,zz}\right),$$

or

$$\Theta_1(r,z,t) = \Theta_1^0(z,t) + r^2\Theta_1^1(z,t), \tag{27}$$

where $\Theta_1^0(z,t) = \Theta_1(0,z,t)$ and using (19a)

$$\Theta_1^1(z,t) = \frac{1}{2R}(R'\Theta_{0,z} - \Theta_0). \tag{28}$$

The function $\Theta_1^1(z,t)$ is known from the data and the zeroth order solution. By adopting the same procedure as for the zeroth order model we can find $\Theta_1^0(z,t)$, i.e., integrating (15b) with respect to r and using the boundary condition at $r = R$ to eliminate $\Theta_{2,r}$. We derive

$$\frac{1}{\mathrm{St}}\Theta_{1,t}^0 - \Theta_{1,zz}^0 = \frac{2}{R}(R'\Theta_{1,z}^0 - \Theta_1^0) + F_1, \qquad 0 < z < S_0(t),\ t > 0, \tag{29a}$$

$$\Theta_{1,z}^0(0,t) = \delta\Theta_1^0(0,t), \qquad t \geq 0, \tag{29b}$$

$$\Theta_1^0(S_0(t),t) = -S_1(0,t)\Theta_{0,z}(S_0(t),t), \qquad t \geq 0, \tag{29c}$$

$$S_1'(r,t) = \left(\Theta_{1,z}^0 + S_1\Theta_{0,zz} + r^2F_2\right)(S_0(t),t), \qquad S_1(r,0) = 0,\ t > 0, \tag{29d}$$

where

(29e)

$$F_1 = -\frac{R^2}{2}\left(\frac{1}{\mathrm{St}}\Theta_{1,t}^1 - \Theta_{1,zz}^1\right) + 2R(R'\Theta_{1,z}^1 - \Theta_1^1) - \frac{R'^2\Theta_0}{R}, \quad F_2 = \Theta_{1,z}^1 + \frac{4(\Theta_1^1)^2}{\Theta_{0,z}},$$

and r appears as a parameter in (29d).

This first order problem (29) has the same structure as the zeroth order problem (19) but is inhomogeneous; i.e., the zeroth order solution provides the forcing (or heating). A further key difference is in the coupling with the crystal-melt interface position S_1. Equation (29c) provides the lower boundary condition for Θ_1 and S_1 advances through (29d), which is consequently a first order quasi-linear partial differential equation.

In general, the coupled system (29) must be solved numerically. For the pseudosteady case, the formula can be simplified as follows. From the definition of Θ_1^1 and using the pseudosteady condition $\Theta_{0,zz} = -4\Theta_1^1$, expressions (29a) and (29d) reduce to

(30)
$$\Theta^0_{1,zz} + \frac{2}{R}(R'\Theta^0_{1,z} - \Theta^0_1) = \frac{1}{4}(2R' + 5R'R'' - RR''')\Theta_{0,z} - \frac{1}{4R}(2R - 4R'^2 + 5RR'')\Theta_0$$

and

(31)
$$S_1'(r,t) = \Theta^0_{1,z} + \frac{2}{R}(1 - R'\Theta_{0,z})S_1 + \frac{r^2}{2R^2}\left(-3R' + (RR'' + R'^2 + R)\Theta_{0,z} + \frac{2}{\Theta_{0,z}}\right),$$

where the right-hand side of (31) is evaluated at $z = S_0(t)$ and r appears as a parameter.

3.2.1. Constant radius crystals. Since $R(z) = R_0$, expression (30) reduces to $\Theta^0_{1,zz} - k^2\Theta^0_1 = -\Theta_0/2$ with $k^2 = 2/R_0$. Solving for Θ^0_1 and using (27)–(28) one finds

$$\Theta_1(r,z,t) = \frac{\cosh kz}{\cosh kS_0}\left[-\Gamma(S_0) - S_1^0\Theta_{0,z}(S_0)\right] + \Gamma(z) - \frac{1}{4}k^2r^2\Theta_0(z)$$

with $S_1^0 = S_1(0,z)$ and

$$\Gamma(z) = \frac{1}{2k}\int_0^z \Theta_0(\xi)\sinh k(\xi - z)\,d\xi.$$

When $\delta = 0$, $\Gamma(z) = -z\sinh kz/4k\cosh kS_0$ yields

$$\Theta_1(r,z,t) = \frac{1}{4k}\frac{\cosh kz}{\cosh kS_0}\left(S_0\tanh kS_0 - z\tanh kz - 4k^2S_1^0\tanh kS_0 - k^3r^2\right).$$

S_1 can be obtained by (29d).

3.2.2. Conical crystals. Since $R(z) = R_0 + \alpha z$, and from (20) $\Theta_1^1 = (\alpha\Theta_{0,z} - \Theta_0)/2R = -\Theta_{0,zz}$, we find

$$\Theta^1_{1,z} = -\left(\frac{3\alpha^2}{2R^2} + \frac{1}{2R}\right)\Theta_{0,z} + \frac{3\alpha}{2R^2}\Theta_0, \quad \Theta^1_{1,zz} = \left(\frac{6\alpha^3}{R^3} + \frac{3\alpha}{R^2}\right)\Theta_{0,z} - \left(\frac{6\alpha^2}{R^3} + \frac{1}{R^2}\right)\Theta_0.$$

Consequently, (30) reduces to

$$\Theta^0_{1,zz} + \frac{2\alpha}{R}\Theta^0_{1,z} - \frac{2}{R}\Theta^0_1 = \frac{\alpha}{2}\Theta_{0,z} + \frac{1}{2R}(2\alpha^2 - R)\Theta_0, \tag{32}$$

and we see that even for the pseudosteady cone, numerical methods will have to be used in general.

Further discussion is deferred to section 5. In the following we turn our discussion to thermal stress inside the crystal.

4. Thermal stress. The thermal stress experienced by the crystal during its growth leads to the generation of structural defects in the crystal [31]. If we want to eliminate these undesirable defects, then one must control the thermal stress. We begin with a brief introduction to the case of an isotropic body. Although InSb is

anisotropic with respect to its elasticity, this will be dealt with in a subsequent section. Fundamentals can be found elsewhere [21, 28].

From the elements of the stress tensor the characteristic amount of stress at a particular position can be described by the von Mises stress σ_{VM} with the relationship

$$2\sigma_{\mathrm{VM}}^2 = (\sigma_1 - \sigma_2)^2 + (\sigma_1 - \sigma_3)^2 + (\sigma_2 - \sigma_3)^2, \tag{33}$$

where σ_1, σ_2, σ_3 are the eigenvalues of the stress tensor. Being a function of the eigenvalues, the von Mises stress is invariant under coordinate transformations.

For a given temperature field, the resulting set of thermoelastic equations for the displacement vector are coupled, and a numerical method will be needed to solve the displacements before thermal stress can be computed. It is instructive to consider the special case where the displacement occurs in one of the three directions, due to the nature of temperature variation. In the following, we will address the thermal stress that arises from temperature variation in the radial direction, as this is the dominant contribution.

4.1. Thermal stress due to radial temperature variation. We assume the displacement vector is of the form $\vec{u} = \langle u(r), 0, 0\rangle$ and converting to nondimensional units u satisfies

$$\frac{\partial}{\partial r}\left[\frac{1}{r}\frac{\partial}{\partial r}(ru)\right] = \epsilon\frac{(1+\nu)}{(1-\nu)}\frac{\partial\Theta_1}{\partial r}, \qquad u(0) < \infty, \quad \sigma_{rr}(R) = 0,$$

where ν is the Poisson ratio. The condition $u(0) < \infty$ is due to the axisymmetry, and since the crystal surface is unstressed, $\sigma_{rr}(R) = 0$. The stress has been nondimensionalized by $\alpha_0\Delta TE/(1-\nu)$, E is the Young's modulus, and α_0 is the coefficient of thermal expansion. We have assumed here that $\Theta_z \simeq 0$ since we want to focus on the sole effect of any radial temperature variations. The solution satisfying the boundary conditions is

$$u(r) = \epsilon\frac{(1+\nu)}{(1-\nu)}\left[\frac{1}{r}\int_0^r \Theta_1(s)s\,ds + (1-2\nu)\frac{r}{R^2}\int_0^R \Theta_1(s)s\,ds\right],$$

and using (27), the corresponding nontrivial stresses are

$$\sigma_{rr} = \epsilon\left[\frac{1}{R^2}\int_0^R \Theta_1(s)s\,ds - \frac{1}{r^2}\int_0^r \Theta_1(s)s\,ds\right] = \frac{1}{4}\epsilon\Theta_1^1\left(R^2 - r^2\right), \tag{34a}$$

$$\sigma_{\theta\theta} = \epsilon\left[\frac{1}{R^2}\int_0^R \Theta_1(s)s\,ds + \frac{1}{r^2}\int_0^r \Theta_1(s)s\,ds - \Theta_1(r)\right] = \frac{1}{4}\epsilon\Theta_1^1\left(R^2 - 3r^2\right), \tag{34b}$$

$$\sigma_{zz} = \epsilon\left[\frac{2}{R^2}\int_0^R \Theta_1(s)s\,ds - \Theta_1(r)\right] = \frac{1}{2}\epsilon\Theta_1^1\left(R^2 - 2r^2\right) \tag{34c}$$

with σ_{zz} modified using St. Venant's principle.

Using (33) to compute the von Mises stress gives

$$\sigma_{\mathrm{VM}}(r,z,t) = \frac{1}{4}\epsilon\left|\Theta_1^1\right| R^2\left[1 - 4\left(\frac{r}{R}\right)^2 + 7\left(\frac{r}{R}\right)^4\right]^{1/2}. \tag{35}$$

The object in the square brackets is a shape factor, and it ranges from a value of

$\sqrt{3/7}$ at a radius of $r = \sqrt{2/7}R(z)$ to a maximum value of two at the outer edge of the crystal. For $\sqrt{4/7}R(z) < r \leq R(z)$ this factor is greater than one.

Remark 1. From (19a) and (28), $\Theta_1^1 = (\Theta_{0,t}/\,\mathrm{St} - \Theta_{0,zz})/4$, which reduces to $|\Theta_1^1| = |\Theta_{0,zz}|/4$ in the pseudosteady limit. This generalizes the classical result that the stress level is a characteristic of the concavity of the temperature in the axial direction [22, 34]. The stress is also linearly proportional to the Biot number ϵ indicating that an increase in the crystal radius will also increase the stress level, other conditions being equal. It also indicates that the increase of radius can be offset by reducing the heat transfer coefficient h_{gs}, suggesting that a possible way to reduce the stress is by changing the local heat flux from the crystal lateral surface.

Remark 2. Also from (28), it is clear that there are two components in the expression for Θ_1^1. Therefore both the temperature gradient and the crystal profile are important for stress reduction. Since circular cylindrical shape is normally adopted for the growth of more common crystals such as silicon, the shape effect has not been discussed much in the literature. However, for crystals such as InSb with relatively low resistance to thermal stress, finding the right shape is often part of an important strategy for growing defect-free crystals. We will address this issue again in later sections.

Remark 3. As other stresses, such as the total resolved stress, are often considered more relevant for causing defects, it is important to point out that the same characteristics remain for different representations of the thermal stress or for crystals being pulled in different directions. These issues will be the topic of the following two subsections.

4.2. Resolved stress. InSb crystallizes in a zincblende or $\bar{4}$3m structure. The structure description is two interpenetrating face-centered cubic (f.c.c.) sublattices of In and Sb separated by the displacement vector $a\langle 1,1,1\rangle/4$. Each In (Sb) atom is tetrahedrally coordinated with an Sb (In) atom. An alternative description of the structure is a f.c.c. sublattice of Sb atoms with one-half of the tetrahedral sites filled with In atoms. The nearest neighbor distance is $\sqrt{3}a/4$ and the lattice parameter is $a = 0.6476$ nm.

The preferred method of dislocation generation in InSb, as in all III-V semiconductors, is through the generation of slip defects, in particular the $\{111\}$, $\langle 1\bar{1}0\rangle$ slip system [19]. This system consists of four glide planes within which atoms can slip in one of three directions. For example, in the (111) plane the slip directions are $[10\bar{1}]$, $[\bar{1}10]$, and $[0\bar{1}1]$. Figure 4 looks down the z-axis of the tetrahedral structure of the crystal and shows each of the 12 permissible glide directions classified into five different categories.

The amount of stress in a particular slip direction $\vec{g}$ within a given glide plane with normal $\vec{n}$ is known as the resolved stress, σ_{RS}. If one assumes the crystallographic axes coincide with the coordinate axes, then σ_{RS} is computed by finding

$$\sigma_{\mathrm{RS}} = \vec{g}^T Q \sigma Q^T \vec{n}, \tag{36}$$

where Q is the coordinate transformation matrix that takes $(r,\theta,z) \to (x,y,z)$ and σ is the stress tensor in the (r,θ,z) coordinates. In summary, the five categories

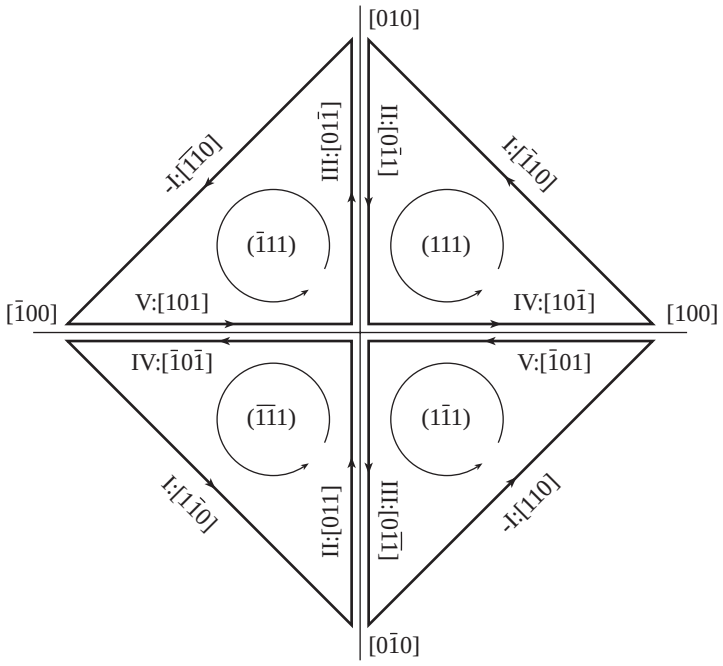

FIG. 4. *Illustrated are each of the* 12 *slip directions in the* $\{111\}$, $\langle 1\bar{1}0\rangle$ *slip system. The roman numerals refer to the functional form of the stress in the direction of the appropriate slip plane.*

illustrated in Figure 4 yield[1]

$$\sigma_{\mathrm{RS}}^{\mathrm{I}} = -\frac{1}{\sqrt{6}}(\sigma_{rr} - \sigma_{\theta\theta})\cos 2\theta, \tag{37a}$$

$$\sigma_{\mathrm{RS}}^{\mathrm{II}} = \frac{1}{\sqrt{6}}[(\sigma_{zz} - \sigma_{\theta\theta}) - (\sigma_{rr} - \sigma_{\theta\theta})(\sin^2\theta + \sin\theta\cos\theta)], \tag{37b}$$

$$\sigma_{\mathrm{RS}}^{\mathrm{III}} = -\frac{1}{\sqrt{6}}[(\sigma_{zz} - \sigma_{\theta\theta}) - (\sigma_{rr} - \sigma_{\theta\theta})(\sin^2\theta - \sin\theta\cos\theta)], \tag{37c}$$

$$\sigma_{\mathrm{RS}}^{\mathrm{IV}} = -\frac{1}{\sqrt{6}}[(\sigma_{zz} - \sigma_{\theta\theta}) - (\sigma_{rr} - \sigma_{\theta\theta})(\cos^2\theta + \sin\theta\cos\theta)], \tag{37d}$$

$$\sigma_{\mathrm{RS}}^{\mathrm{V}} = \frac{1}{\sqrt{6}}[(\sigma_{zz} - \sigma_{\theta\theta}) - (\sigma_{rr} - \sigma_{\theta\theta})(\cos^2\theta - \sin\theta\cos\theta)]. \tag{37e}$$

Plastic deformation of the crystal occurs if the stress in any of the 12 slip directions exceeds the critical resolved shear stress, σ_{crss}. To leading order, the actual density of dislocations suffered by the crystal is proportional to the total excess stress at any given point within the crystal. In this sense, an estimation of where dislocations are likely to occur is given by the distribution of the total absolute stress:

$$|\sigma_{\mathrm{tot}}| = 4\left|\sigma_{\mathrm{RS}}^{\mathrm{I}}\right| + 2\left(\left|\sigma_{\mathrm{RS}}^{\mathrm{II}}\right| + \left|\sigma_{\mathrm{RS}}^{\mathrm{III}}\right| + \left|\sigma_{\mathrm{RS}}^{\mathrm{IV}}\right| + \left|\sigma_{\mathrm{RS}}^{\mathrm{V}}\right|\right). \tag{38}$$

An additional complication is that, in general, the elastic constants depend on the solidification direction since the thermal and crystallographic axes are not aligned. However, for crystals that belong to the cubic classes this does not play a role [2].

[1]Note: $\theta = -\varphi$, where φ is the angular coordinate used by Jordan, Caruso, and von Neida [19].

4.3. Crystal extraction in an arbitrary direction. The previous subsection supposes the crystal is extracted from the melt in a direction coincident with the crystallographic axes. If there is a misalignment between the frame defined by the crystallographic axes of the unit cell and the frame with its z-axis coincident with the solidification direction, then a coordinate transformation is required to align $\vec{n}$ and $\vec{g}$. These directions must change because they are with respect to the crystallographic axes and not the the temperature field that determines the stress tensor. Let U_{v_p} denote a coordinate transformation, depending on the pulling direction, that takes vectors in the crystallographic frame to the solidification frame. The total resolved stress of the $\{111\}$, $\langle 1\bar{1}0\rangle$ slip system becomes

$$|\sigma_{\text{tot}}| = \sum_{i=1}^{12} \left| \vec{g}_i^T U_{v_p}^T Q \sigma Q^T U_{v_p} \vec{n}_i \right|, \tag{39}$$

where the symmetry in expression (38) has been broken.

5. Numerical results and discussion. We first discuss the temperature solutions for the decoupled growth; i.e., the heat flux from the melt to the crystal is assumed a known (constant) value. In particular, we compare the pseudosteady $\big($(19), (29) with $\Theta_{0,t} = \Theta_{1,t}^0 = \Theta_{1,t}^1 = 0\big)$ and the unsteady solution (12). Even though the Stefan number is not much bigger than unity, the results show that the pseudosteady solutions are in good agreement with the unsteady calculation. This indicates that the thermal stress can be reasonably estimated using the pseudosteady solution, which greatly simplifies the calculation. The case for coupled growth is also investigated, and we show the transient influence of the melt is only important towards the end of the growth. During the growth, the heat flux from the melt to the crystal changes slowly, suggesting that the temperature solutions for the decoupled case are good approximations. The thermal stress is computed based on the pseudosteady solution using the decoupled growth condition for simplicity.

Table 2 displays the various quantities used in the simulation and not found in the previous table.[2]

5.1. Temperature solutions.

5.1.1. Decoupled growth. In this section we attempt to justify the pseudosteady approximation. To begin, we assume $\gamma = \delta = 0$, decoupling the crystal from the melt in the crucible. Figure 5 compares the time dependence of the position of the crystal-melt interface $S(r,t)$ using (12) (the unsteady case) with its zeroth order approximation $S_0(t)$ using (20), (19b)–(19d) (the pseudosteady case). To determine the influence of both the crystal profile and the amount of heat transfer, a cylindrical and conical profile were assumed and, for each profile, two values of ϵ ($\epsilon_1 = 0.0066$, $\epsilon_2 = 0.026$) were considered. Using only the zeroth order approximation, the interface position is uniformly overestimated with the pseudosteady approximation, and the amount of overestimate is proportional to ϵ. The largest relative difference is about 10% and occurs at the end of the growth for a cylindrical crystal with the largest value of ϵ.

The radial dependence of the interface can be estimated with the first order perturbation, $S_0(t) + \epsilon S_1(r,t)$. Figure 6 compares this approximation with the radial de-

[2] h_{sl} and h_{cl} are based on estimated boundary layer thicknesses of 2.5 mm and 1.8 mm, respectively. The former is due to an Ekman layer (rotations of crucible and the crystal at 5 rpm) and the latter is due to natural convection ($\Delta T = 1$ K, $\nu = 3.3 \times 10^{-7}$ m^2/s, Grashof number $\simeq 6.0 \times 10^6$).

TABLE 2
Remaining liquid and growth parameters used in the simulations.

Data	Symbol	Value
Growing properties		
Ambient temperature	T_a	600 K
Seed radius	R_0	0.005 m
Seed length	Z_0	0.03 m
Crucible depth	$\tilde{Z}_c$	0.0875 m
Crucible radius	$\tilde{R}_c$	0.0875 m
Thermal expansion	α_0	5.5×10^{-6} /K
Liquid properties at $T = T_m$		
Density	ρ_l	6.47×10^3 kg/m^3
Thermal conductivity	k_l	9.23 W/m K
Heat capacity	$\rho_l c_l$	1.7×10^6 J/m^3 K
Heat transfer coefficients		
Solid-liquid	h_{sl}	3700 W/m^2 K
Gas-liquid	h_{gl}	2 W/m^2 K
Crucible-liquid	h_{cl}	5230 W/m^2 K

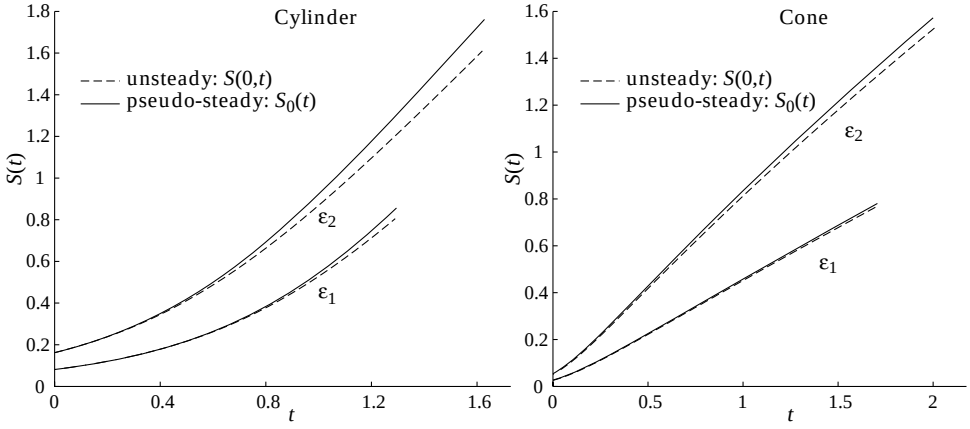

FIG. 5. *Time evolution of $S_0(t)$ for the pseudosteady approximation compared with $S(0,t)$. For both values of ϵ and both crystal profiles $S_0(t)$ closely approximates $S(0,t)$.*

pendence obtained by solving the unsteady equations at the end of the crystal growth, $t = t_f$. In both the case of a cylindrical and a conical crystal the growth interface is convex (viewed from inside the crystal). For the conical crystal the interface is flatter even though the curvature grows with time for both cases. The pseudosteady results closely track the unsteady solution with a maximum relative difference less than 5%.

As a final comparison, Figures 7 and 8 display the predicted thermal profile for the cylindrical and conical crystals, respectively. The crystals are displayed in the physically correct aspect ratio and with their respective solid-liquid interface. It can be seen that the pseudosteady and unsteady solutions are in close agreement.

From the previous results it is clear that without any coupling from the melt, the pseudosteady solution approximates the solution of the fully time dependent Stefan problem. When one considers coupling the melt in the crucible with the crystal, the pseudosteady approximation will remain valid if the predicted heat flux from the melt does not change appreciably over the growth of the crystal. In this case the temperature and flux of the melt are determined by (13).

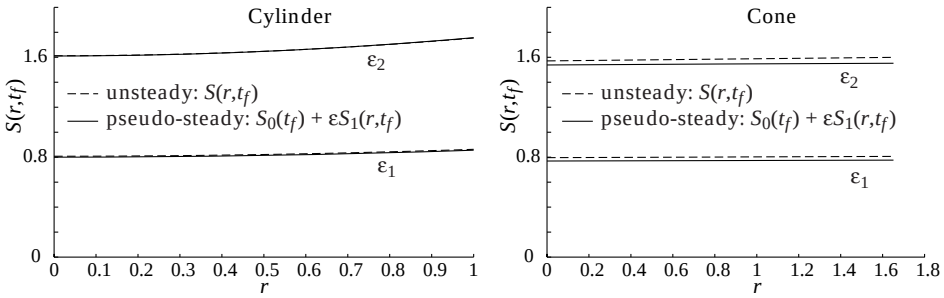

FIG. 6. *Comparison of the radial dependence of interface at the end of growth for the unsteady* $\left(S(r,t_f)\right)$ *and the first order approximation pseudosteady* $\left(S_0(r,t_f)+\epsilon S_1(r,t_f)\right)$ *cases.*

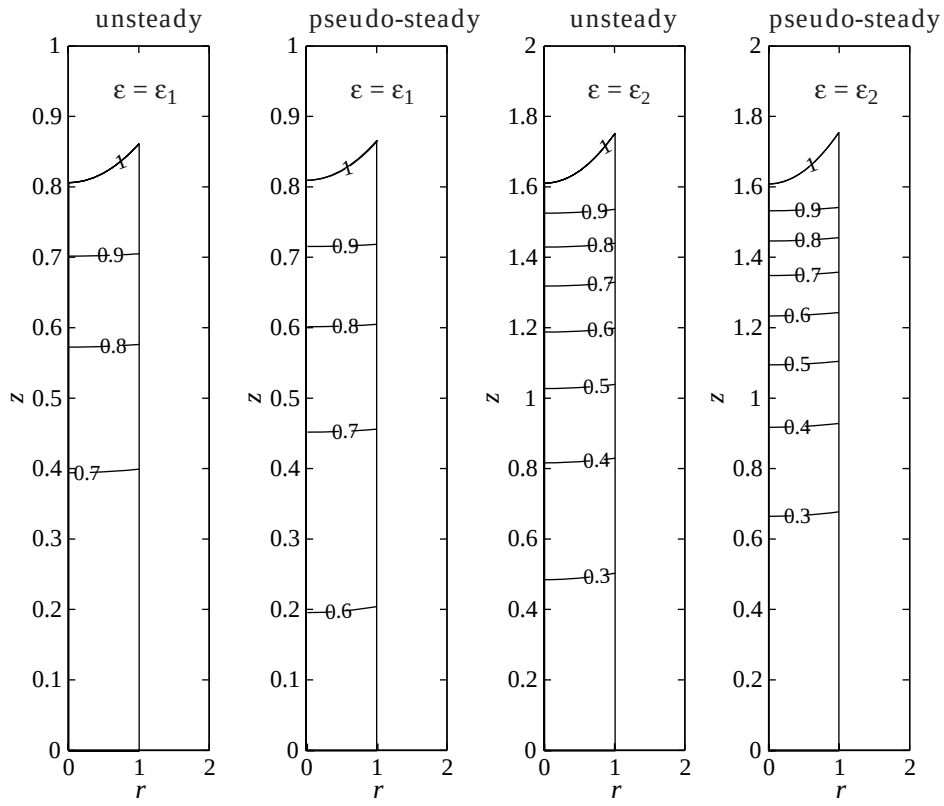

FIG. 7. *Nondimensional temperature contours for the cylinder at the end of the growth illustrated at the correct aspect ratio.*

5.1.2. Coupled growth with melt in the crucible. In this simulation we solve (19) with a cylindrical seed where $\gamma = \gamma(t)$ as determined by (13). In addition, $h_{gs} = 4$, $\delta = 0$, and the remaining heat transfer coefficients are listed in Table 2. Results for a cylindrical and conical crystal pulled from a parabolic crucible $\left(z = \tilde{Z}_c(r/\tilde{R}_c)^2\right)$ are displayed in Figure 9. In both cases the temperature of the crucible was initially $T_c(0) = T_m + 0.046$ K (dimensional) and reduced at a constant rate of

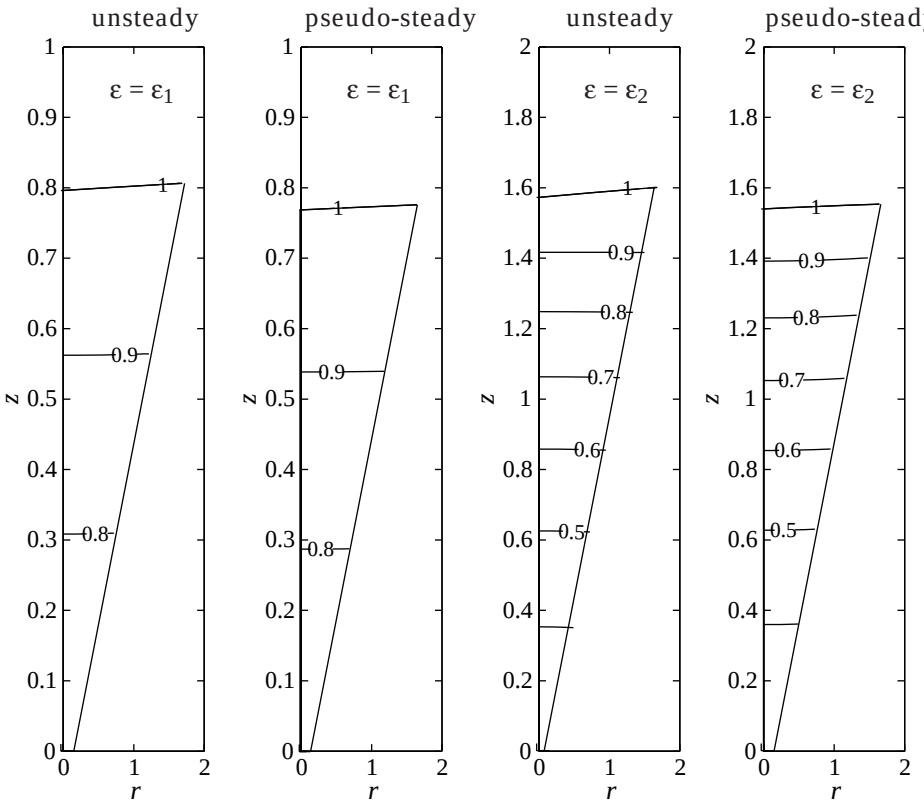

FIG. 8. *Nondimensional temperature contours for the cone at the end of the growth illustrated at the correct aspect ratio.*

0.2 K/hr.

On the far left of Figure 9 the grown crystal is illustrated at the physically correct aspect ratio with the initial and final melt levels. The initial level is chosen so that 25% of the melt remains in the crucible once the crystal achieves its final length. Growth times for each crystal are indicated on the far right.

The center two images display the time evolution of the crystal temperature with the pseudosteady position (St $\to \infty$) of the interface indicated with crosses. For the cylindrical case the initial rapid increase in the radius imprints an echo of the seed into the thermal field which will increase the stress in the shoulder of the crystal. Such an effect has recently been described elsewhere [22]. The dashed lines show the solution if $\gamma = 0$. By setting γ constant the growth rate of the crystal becomes essentially constant rather than accelerating as seen in the coupled case.

The far right shows the growth rate of the interface $S_0'(t)$, the corresponding pull rate $v_p(t)$, and the rate at which the melt drops $\lambda^2 v_m(t)$. For the cylindrical crystal, the growth rate rapidly decreases as the crystal shoulder is formed from the initial seed. This effect is decreased for the conical crystal, leading to a more uniform pull rate with this profile. As the crucible empties, the melt falls more rapidly, causing the pulling speed to reduce near the end of the growth. For the cone this is emphasized as the cross-sectional area increases with time.

Figure 10 illustrates both $\gamma(t)$ and the components of expression (13) during the

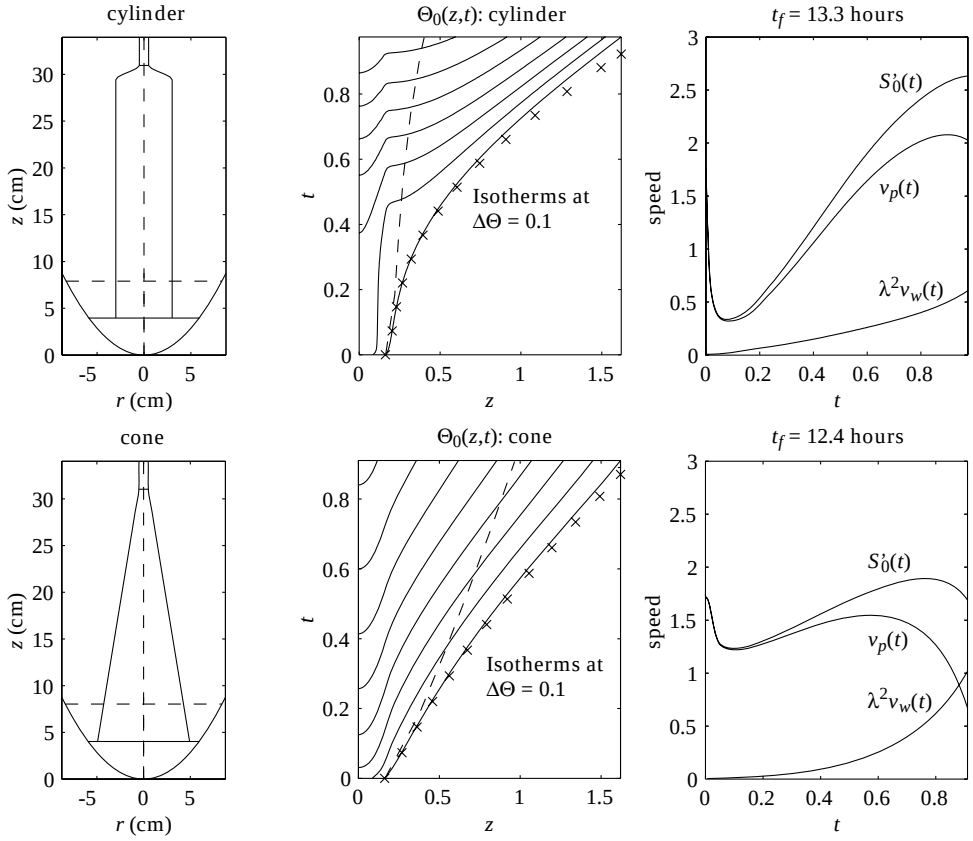

FIG. 9. *Final configuration of the crystal-melt system, thermal fields, and interface speeds for the coupled system* (13) *and* (19). *On the left is the final crystal position in the furnace. The temperature field is detailed in the center and the interfacial velocities are displayed to the right. Cylindrical and conical growth are on the top and bottom rows, respectively.*

growth cycle for the cylindrical and conical crystal profiles. The flux from the melt $\gamma(t)$ is shown to the left of the figure. Changes in the flux are driven primarily by the chosen rate of change of the crucible temperature and is relatively insensitive to the crystal profile. In both cases the magnitude of undercooling was $\simeq 2$ K. A more sophisticated model that considers the dynamics of the melt is clearly required to quantitatively estimate any undercooling effects. This research is currently underway.

Even with our very simple model for the melt, two separate growth regimes are clearly identified. By considering the source of the various heat fluxes acting on the melt one observes that in the initial states of growth, the heat loss to the ambient gas $Q_{gl} = h_{gl}(A_c - A)(T_l - T_g)$ and the heat gain from the crucible $Q_{cl} = h_{cl}A_l(T_c - T_l)$ are the dominant terms in (13). Once the crucible is cool enough, it becomes the dominant channel for heat loss, whereas the melt is heated by the solid-liquid interface at T_m and the decreased heat capacity through volume loss of the melt. The profile of the crystal changes $Q_{sl} = h_{sl}A(T_l - T_m)$ and Q_{gl}, while the shape of the crucible governs the behavior of Q_{cl}. $Q_{vl} = -\rho_l c_l T_l V_l'$ is dictated by the rate of growth. The nondimensional quantities in Figure 10 are found by dividing the Q_i by the dimensional factor $\tilde{R}_c{}^2 \tilde{Z}_c h_{gs} \Delta T / \overline{R}$.

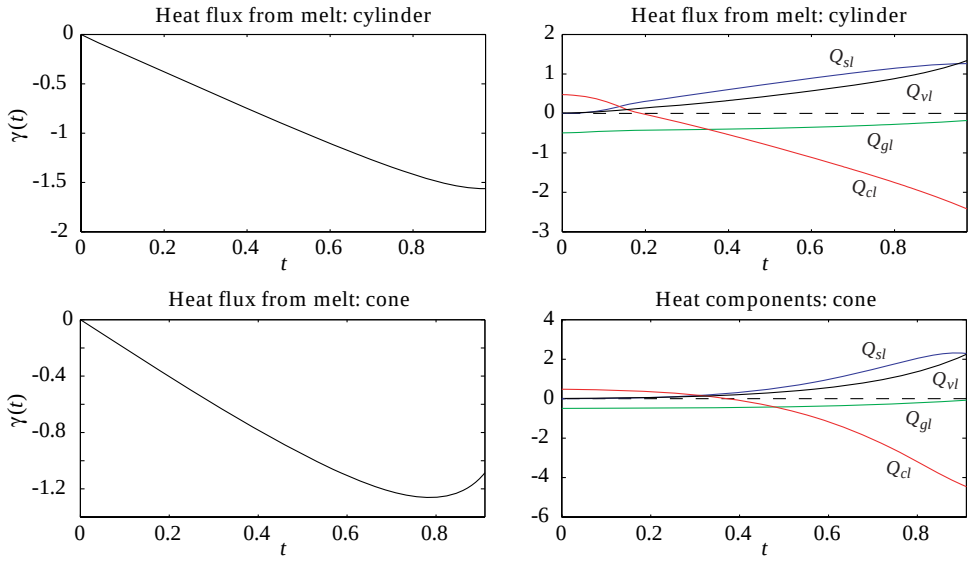

FIG. 10. *The nondimensional flux and the heat flux components of expression* (13) *through the growth cycle. The various components detailed to the right are discussed in section* 5.1.2.

5.2. Thermal stress. For an anisotropic crystal, Young's modulus E and Poisson's ratio ν depend on the specific orientation of the crystal. However, these values are invariant within the {111} planes [2]. For InSb one has

$$E_{\{111\}} = \frac{4(C_{11}+2C_{12})(C_{11}-C_{12})C_{44}}{(C_{11}+2C_{12})(C_{11}-C_{12})+2C_{11}C_{44}} = 6.18\times 10^4 \text{ MPa},$$
$$\nu_{\{111\}} = \frac{1}{3}\frac{(C_{11}+2C_{12})(C_{11}-C_{12})-2C_{44}(C_{11}-4C_{12})}{(C_{11}+2C_{12})(C_{11}-C_{12})+2C_{11}C_{44}} = 0.364,$$

where $C_{11} = 6.70\times 10^4$, $C_{12} = 3.65\times 10^4$, $C_{44} = 3.02\times 10^4$ are crystal stiffness constants[3] in MPa and, consequently, the dimensional constant for the stress calculations is $\alpha_0 \Delta T E/(1-\nu) \simeq 107$ MPa.

Figure 11 shows the stress contours of the von Mises stress for the cylinder and the cone at the end of the growth corresponding to the pseudosteady results in Figures 7 and 8. For a fixed value of ϵ the stress in the conical case is about one-half that of the cylindrical case. Also, increasing ϵ increases the stress level dramatically. By growing a conical crystal the stress can be reduced significantly. For a given temperature the amount of stress at which crystal deformation begins to occur is known as the critical resolved shear stress, σ_{crss}. In the case of InSb, σ_{crss} varies from 0.245 MPa [25] to 4.90 MPa [6] as the temperature varies from $T_m = 798.4$ K to 491 K, respectively, indicating that the conical crystal remains below this critical stress level.

An additional method of reducing the stress level in the crystal is to use the anisotropic nature of the crystal to our advantage by changing the direction in which the crystal is solidified. From expression (39) one can see that for a fixed vertical position in the crystal the total absolute resolved stress is a complicated function of

[3]The corresponding compliances are $S_{11} = 2.42\times 10^{-5}$ MPa^{-1}, $S_{12} = -8.55\times 10^{-6}$ MPa^{-1}, $S_{44} = 3.31\times 10^{-5}$ MPa^{-1}.

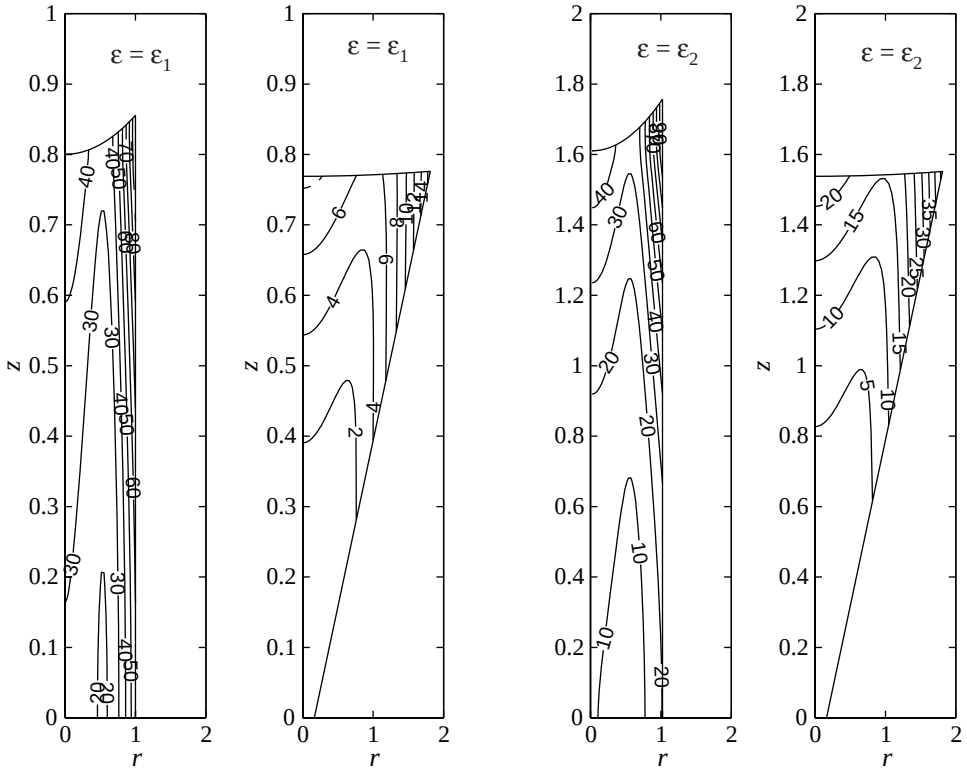

FIG. 11. *von Mises stress for the pseudosteady cylindrical and conical crystal cases. Isostress contours are labeled as a percent of the maximum stress (*0.176 *MPa for* ϵ_1 *and* 0.706 *MPa for* ϵ_2*).*

the angular coordinate. Figure 12 shows the stress pattern for a cylindrical crystal just inside the crystal-melt interface when the crystal is pulled in the directions [001], [111], [10$\bar{1}$], and [$\bar{1}$2$\bar{1}$] respectively. The temperature field corresponds to values of $h_{gs} = 4$, $\gamma = 0$, and $\delta = 0$ grown with the pseudosteady approximation. The $\langle 211 \rangle$ directions are preferred growth directions [23]. The other directions are for comparative purposes. Notice that the isostress contours are square for the [001] direction and hexagonal for the [111] direction, while the [$\bar{1}$2$\bar{1}$] direction generates distorted rectangular isostress curves. If one assumes that the crystal will solidify in a manner consistent with minimizing the surface stress, then these curves should somewhat approximate the actual cross-sectional shape of the crystal as it is pulled from the melt. Clearly the crystal orientation can significantly reduce the stress. However, not all growth directions are amenable to crystal growth [23]. Because of these other issues, changes in the growth orientation are more effective at redistributing the stress within a particular cross-section than reducing the overall magnitude of stress. The issue of optimizing the growth conditions will be addressed in a subsequent paper.

6. Conclusion. In this study, we present a semianalytical approach for the temperature and thermal stress inside an InSb crystal. The purpose of the paper is twofold. By identifying the main physical features and using suitable mathematical models, we have gained useful insights into this complex manufacturing process. In particular, we have determined the dependence of the crystal stress on the evolving

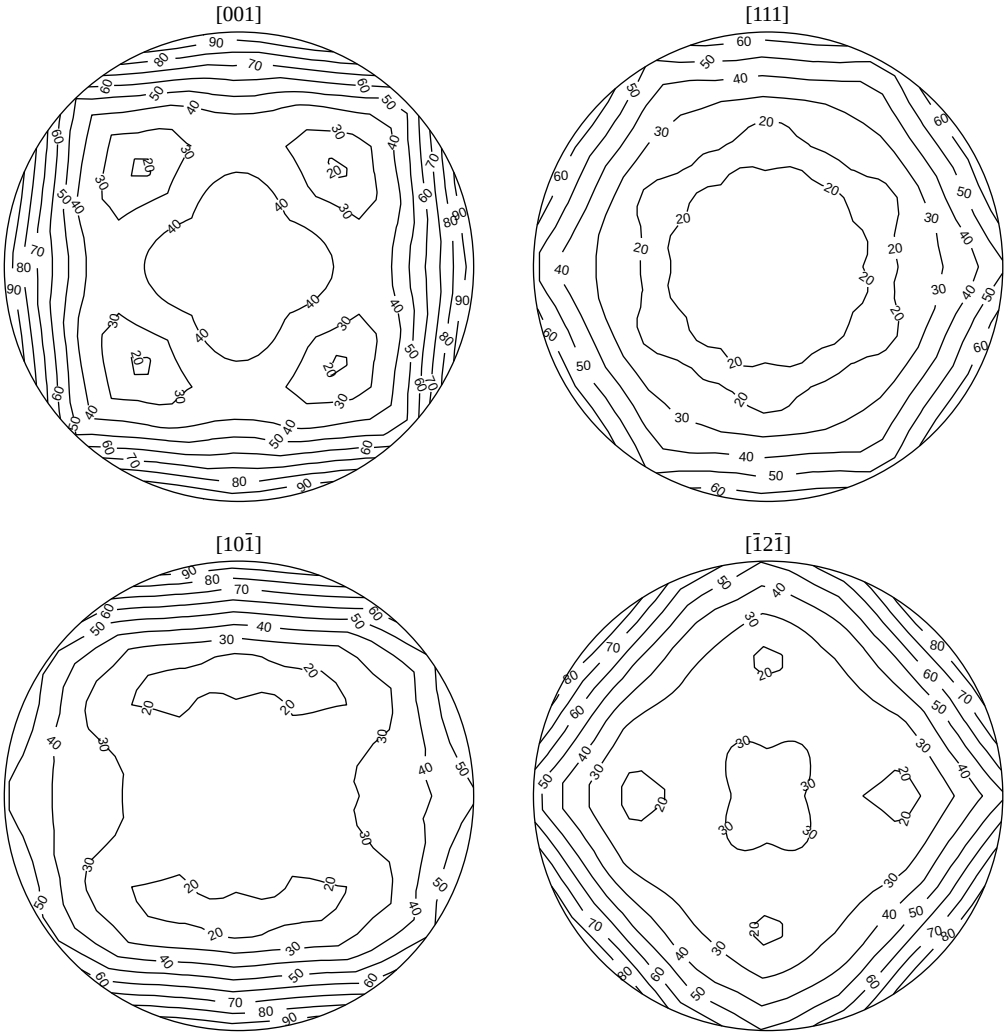

FIG. 12. *Total resolved stress distribution, computed using* (39)*, for a cylindrical crystal, at the indicated orientation, just inside the crystal-melt interface at the end of the growth. All reported stress values are expressed in percent with* 100% *occurring at the outer edge of a crystal grown in the* [001] *direction.*

crystal profile. By deriving semianalytical solutions, we have also provided a base that can be used to search for suitable growth conditions to improve the manufacturing procedure for all III-V compounds.

An important feature of our approach is that it allows us to derive explicit relationships between the thermal stress and relevant physical and geometrical parameters. This is achieved by using an asymptotic expansion of the solution in terms of the Biot number, characterizing the lateral heat flux. The asymptotic solution is obtained by solving essentially one-dimensional problems. The results show that the stress induced by radial temperature variation is related to the size (radius) and the profile (variation of the radius) of the crystal and heat flux through the side surface. On the other hand, the influence of the crystal radius on the stress induced by the

axial temperature variation is much weaker. The heat flux through the side surface is an important factor for reducing the overall thermal stress inside the crystal. The explicit nature of the thermal stress allows for a more efficient optimal control approach for finding better growth conditions, as shown in [15].

The other advantage of our semianalytical approach is that it can be extended to cases with more complicated models for the melt and gas flows. For example, the effect of the gas flow on the lateral heat flux between the crystal surface and the gas can be modeled by a nonconstant heat exchange coefficient h_{gs}. The motion of the melt can also be modeled by a similar approach, using a boundary layer argument [8, 9] or by solving the Navier–Stokes equations and temperature equation numerically. These will be the subject of a subsequent paper.

As pointed out earlier, we have assumed that the pulling rate can be adjusted to grow a crystal with a desirable shape. In practice, we may need to consider the dynamics and stability of the radial motion of the three-phase triple point. Models and computations have been carried out to capture the motion of the three-phase contact point [7, 32] and can be incorporated with the current model in a straightforward fashion. This work is currently underway.

Finally, we note that our study has its limitations and there is room for improvements and future investigations. For example, a nonuniform heat flux from the melt will introduce radial variation in the zeroth order temperature solution. As a result, the thermal stress will be determined not only by the axial gradient of the zeroth order solution but its radial variation as well. However, this radial variation is likely to be small, from our own observations and others, and an asymptotic solution can also be obtained, as indicated in [20]. Furthermore, we have not discussed the validity of the plane strain assumption. We believe that an asymptotic argument similar to that used for the temperature can be employed to derive the plane strain solution as part of the asymptotic series. We plan to address this issue also in a future study. Finally, the crystal grown in practice is not axisymmetric. It would be of practical interest to investigate the effect of anisotropy. Study is currently underway for a weakly anisotropic crystal.

Appendix: A simple model for the melt temperature. Starting with dimensional variables, we consider crystal growth in an axisymmetric setting where the rate of growth is small. We assume that the melt (liquid) in the crucible is well mixed and the temperature of the melt, $T_l(t)$, is uniform in space except in the thin layers near the crystal-melt and melt-ambient gas interfaces. We also assume that the ambient gas is well mixed and the temperature of the gas is a constant T_g. Furthermore, we will neglect the shape of the meniscus and assume that the crystal-melt and melt-gas interfaces are flat.[4] Therefore by adjusting the pulling speed v_p, the positions of the crystal-melt and melt-gas interfaces can be described by a single function $z = S(t)$.[5] Finally, we assume that the crystal radius $R(z)$ varies slowly in the z direction, $|R_z| \ll 1$. The coordinate system is fixed to the top of the growing crystal at $z = 0$, as described previously.

Figure 13 shows the three surfaces through which the melt can transfer heat

[4]For InSb crystals under consideration here, the typical length scale is $\overline{R} = 0.03$ m, the surface tension coefficient between the melt and gas is $\sigma_{gl} = 0.434$ N/m, and the melt density is $\rho_l = 6.47 \times 10^3$ kg/m^3. The Bond number is Bo $= \rho_l g \overline{R}^2/\sigma_{gl} \simeq 132 \gg 1$. Thus the meniscus is dominated by the gravity effect and the meniscus changes shape only near the three-phase contact point with a small capillary rise.

[5]The flat interface assumption allows one to drop the explicit r dependence of $S(t)$.

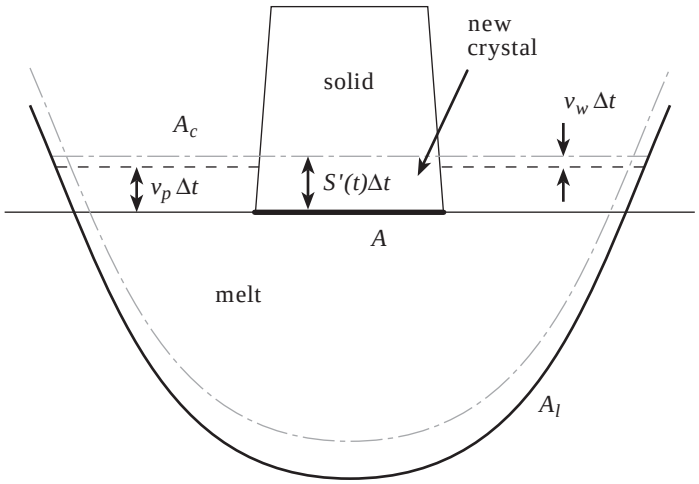

FIG. 13. *For a small time interval Δt the new crystal extends a distance $S'(t)\Delta t$ beyond the original interface location (dashed-dotted line). The corresponding drop in the melt is $v_m\Delta t$ (dashed line), and to realign the melt-gas interface and the crystal-melt the crystal must be extracted an additional distance of $v_p\Delta t$ (solid line).*

energy. These are denoted as $A = \pi R^2$, the area of the crystal-melt interface; $A_c = \pi R_c^2$, the cross-sectional area of the crucible ($A_c - A$ is the area of the melt-gas interface); and A_l, the surface area of the crucible in contact with the melt. Continuing to refer to the figure, conservation of mass implies that the rate at which the melt-gas interface drops due to the change in density upon solidification is

$$v_m(t) = \frac{\rho_s A}{\rho_l A_c} S'(t). \tag{40}$$

To ensure that the crystal-melt interface remains at the surface of the liquid the crucible is dropped at an optimal pull rate

$$v_p(t) = (S' - v_m)(t) = \frac{\rho_l A_c - \rho_s A}{\rho_l A_c} S'(t). \tag{41}$$

If the actual pull rate of the crystal exceeds v_p by a moderate amount, then the surface tension of the melt will cause the radius of the crystal to decrease. Similarly, pulling at a rate slower than v_p will cause the radius to increase.

Using these velocities, the position of the crystal-melt interface is $S = Z_0 + u_w + u_p$, where

$$u_w(t) = \int_0^t v_m(\tau)\, d\tau, \qquad u_p(t) = \int_0^t v_p(\tau)\, d\tau \tag{42}$$

are the displacements due to the loss of melt during the solidification and the growth of the crystal, respectively. The top of the crystal is fixed at $z = 0$.

During the growth period we assume that the heat flux from the melt to the crystal is given by

$$q_l = h_{sl}(T_l - T_m). \tag{43}$$

As a result the heat balance inside the melt yields

$$\frac{d}{dt}\left(\rho_l c_l T_l V_l\right) = -q_l A - h_{gl}(A_c - A)(T_l - T_g) + h_{cl} A_l (T_c - T_l), \tag{44}$$

where V_l is the time dependent volume of the melt, and T_c is the temperature of the crucible. The last term in (44) is the heat flux from the crucible to the liquid and is assumed to be a control parameter with T_c acting as the control.

For simulations in section 5.1.2 the crucible was assumed to be parabolic and filled to the extent that once the crystal reaches its final mass $\rho_s V_{\text{xtal}}$ and growth stops, there is a given proportion, p, of melt mass left in the crucible. As a result, $R_c(\xi) = \tilde{R}_c(\xi/\tilde{Z}_c)^{1/2}$, $0 \le \xi \le \tilde{Z}_c$, and the initial depth of the melt Z_{c0} is determined with the condition

$$\frac{\rho_s}{\rho_l} V_{\text{xtal}} = (1-p)\int_0^{Z_{c0}} \pi R_c^2(\xi)\, d\xi. \tag{45}$$

Since the shape of the crucible is known, A_l and V_l can be obtained as

$$A_l(t) = \int_0^{Z_{c0}-u_w(t)} 2\pi R_c(\xi)\sqrt{1+R_c'^2(\xi)}\, d\xi, \quad V_l(t) = \int_0^{Z_{c0}-u_w(t)} \pi R_c^2(\xi)\, d\xi \tag{46}$$

computed with respect to a local coordinate system fixed to the bottom of the crucible.

A nondimensionalized version of (44) is obtained by substituting the characteristic radius $\tilde{R}_c$ and depth $\tilde{Z}_c$ for the crucible so that

$$R_c = \tilde{R}_c \hat{R}_c, \qquad A = \overline{R}^2 \hat{A}, \qquad A_c = \tilde{R}_c^2 \hat{A}_c, \qquad A_l = \tilde{R}_c \tilde{Z}_c \hat{A}_l, \qquad V_l = \tilde{R}_c^2 \tilde{Z}_c \hat{V}_l.$$

Letting $T_l = T_g + \Delta T \Theta_l$ and $T_c = T_g + \Delta T \Theta_c$ and defining $\lambda = \overline{R}/\tilde{R}_c, \mu = \tilde{R}_c/\tilde{Z}_c, \phi = \rho_l c_l/\rho_s c_s$ one obtains

$$\frac{\phi}{\lambda\,\mathrm{St}}\frac{d}{d\hat{t}}\left[\left(\frac{T_g}{\Delta T}+\Theta_l\right)\hat{V}_l\right] = -\mu\lambda^2\hat{A}\frac{h_{sl}}{h_{gs}}(\Theta_l - 1) - \mu\frac{h_{gl}}{h_{gs}}(\hat{A}_c - \lambda^2\hat{A})\Theta_l + \frac{h_{cl}}{h_{gs}}\hat{A}_l(\Theta_c - \Theta_l) \tag{47a}$$

with $\Theta_l(0) = 1$ and a nondimensional heat flux given by

$$\gamma = \frac{q_{l,n}\overline{R}}{\epsilon^{1/2} k_s \Delta T} = \epsilon^{1/2}\frac{h_{sl}}{h_{gs}}(\Theta_l - 1). \tag{47b}$$

When commencing, the growth of the seed is slowly dropped until it contacts the melt surface and a meniscus is supported. Once the meniscus stabilizes and the seed reaches a thermal equilibrium with the melt and the crystal, the seed is extracted and the furnace temperature is slowly decreased [23]. Assuming a cylindrical seed of length Z_0 and radius R_0 and using expression (22) one finds an initial interface speed of

$$S_0'(0) = k\frac{k\sinh(kZ_0) + \delta\cosh(kZ_0) - \delta\Theta_{ch}}{k\cosh(kZ_0) + \delta\sinh(kZ_0)} \tag{47c}$$

with $k^2 = 2/R_0$. The initial crucible temperature is chosen so that $\Theta_l'(0) = 0$ and from (47a) one has

$$\Theta_c(0) = \left[1 + \mu\frac{h_{gl}}{h_{cl}}\left(\frac{\hat{A}_c - \lambda^2\hat{A}}{\hat{A}_l}\right) + \frac{\phi}{\lambda\,\mathrm{St}}\frac{h_{gs}}{h_{cl}}\frac{1}{\hat{A}_l}\frac{d\hat{V}_l}{d\hat{t}}\left(\frac{T_g}{\Delta T}+1\right)\right](0). \tag{47d}$$

To simulate the cooling of the furnace the crucible temperature was dropped at a constant rate of 0.2 K/hr for all simulations.

Nondimensional versions of the interface speeds (40)–(41), displacements (42), initial depth condition (45), and geometrical factors (46) are derived using the substitutions

$$Z_{c0} = \tilde{Z}_c \hat{Z}_{c0}, \qquad \epsilon^{1/2} u_p = \overline{R} \hat{u}_p, \qquad \epsilon^{1/2} u_w = \lambda^3 \tilde{R}_c \hat{u}_w.$$

Acknowledgments. The authors wish to thank Bill Micklethwaite and his engineers at Firebird Semiconductors Ltd. for sharing their insights and many stimulating discussions. We are also grateful to the anonymous referees for their comments and suggestions.

REFERENCES

[1] H. Alexander and P. Hassen (1968), *Dislocation and plastic flow in the diamond structure*, Solid State Physics, 22, pp. 27–158.
[2] W. A. Brantley (1973), *Calculated elastic constraints for stress problems associated with semiconductor devices*, J. Appl. Phys., 44, pp. 534–535.
[3] K. Brattkus and S. H. Davis (1988), *Directional solidification with heat losses*, J. Crystal Growth, 91, pp. 538–556.
[4] R. A. Brown (1988), *Theory of transport processes in single crystal growth from the melt*, AIChE J., 34, pp. 881–911.
[5] Y. T. Chan, H. J. Gilbeling, and H. L. Grubin (1988), *Numerical simulation of Czochralski growth*, J. Appl. Phys., 64, pp. 1425–1439.
[6] A. R. Chaudhuri, J. R. Patel, and L. G. Rubin (1962), *Velocities and densities of dislocations in germanium and other semiconductor crystals*, J. Appl. Phys., 33, pp. 2736–2746.
[7] A. B. Crowley (1983), *Mathematical modeling of heat flow in Czochralski crystal pulling*, IMA J. Appl. Math., 30, pp. 173–189.
[8] P. A. Davidson (1993), *Similarities in the structure of swirling and buoyancy-driven flows*, J. Fluid Mech., 252, pp. 357–382.
[9] P. A. Davidson and S. C. Flood (1994), *Natural convection in an aluminum ingot: A mathematical model*, Metallurgical and Materials Transactions B, 25, pp. 293–302.
[10] J. J. Derby and R. A. Brown (1988), *On the quasi-steady-state assumption in modeling Czochralski crystal growth*, J. Crystal Growth, 87, pp. 251–260.
[11] F. Dupret and N. van den Bogaert (1994), *Modelling Bridgeman and Czochralski growth*, in Handbook of Crystal Growth, Vol. 2B, D. T. J. Hurle, ed., North–Holland, Amsterdam, pp. 875–1010.
[12] A. Friedman (1964), *Partial Differential Equations of Parabolic Type*, Prentice–Hall, Englewood Cliffs, NJ.
[13] A. N. Gulluoglu and C. T. Tsai (1999), *Effect of growth parameters on dislocation generation in InP single crystal grown by the vertical gradient freeze process*, Acta Materialia, 47, pp. 2313–2322.
[14] S. I. Hariharan and G. W. Young (2001), *Comparison of asymptotic solutions of a phase-field model to a sharp-interface model*, SIAM J. Appl. Math., 62, pp. 244–263.
[15] H. Huang and S. Liang, *An optimal control approach for thermal stress reduction inside a Cz grown crystal*, J. Engrg. Math., submitted.
[16] D. T. J. Hurle, ed. (1993), *Handbook of Crystal Growth, Vol.* 1: *Fundamentals*, North–Holland, Amsterdam.
[17] D. T. J. Hurle, ed. (1994), *Handbook of Crystal Growth, Vol.* 2: *Bulk Crystal Growth*, North–Holland, Amsterdam.
[18] D. T. J. Hurle (1993), *Crystal Pulling from the Melt*, Springer-Verlag, Berlin.
[19] A. S. Jordan, R. Caruso, and A. R. von Neida (1980), *A thermoelastic analysis of dislocation generation in pulled GaAs crystals*, Bell System Tech. J., 59, pp. 593–637.
[20] H. K. Kuiken and P. J. Roksnoer (1979), *Analysis of the temperature distribution in FZ silicon crystals*, J. Crystal Growth, 47, pp. 29–42.
[21] L. D. Landau and E. M. Lifshitz (1970), *Theory of Elasticity*, 2nd ed. Pergamon Press, Oxford, UK.

[22] O. A. Louchev, S. Kumaragurubaran, S. Takekawa, and K. Kitamura (2004), *Thermally induced effects during initial stage crystal growth from melts*, J. Crystal Growth, 273, pp. 320–328.
[23] W. F. Micklethwaite (2003), *private communications*, Firebird Semiconductors Ltd.
[24] W. F. Micklethwaite and A. J. Johnson (2000), *InSb Materials and devices*, in Infrared Detectors and Emitters: Materials and Devices, P. Capper and C. T. Elliot, eds., Kluwer Academic Publishers, Boston, pp. 177–204.
[25] M. G. Mil'vidskii and E. P. Bochkarev (1978), *Creation of defects during the growth of semiconductor single crystals and films*, J. Crystal Growth, 44, pp. 61–74.
[26] G. Müller (2002), *Experimental analysis and modeling of melt growth processes*, J. Crystal Growth, 237-239, pp. 1628–1637.
[27] G. Müller (1988), *Convection and Inhomogeneities in Crystal Growth from the Melt*, Crystals: Growth, Properties and Applications 12, H. C. Freyhardt, ed., Springer-Verlag, Berlin.
[28] J. L. Nowinski (1978), *Theory of Thermoelasticity with Applications*, Sijthoff & Noordhoff International Publishers, Alphen aan den Rijn, The Netherlands.
[29] V. Prasad, H. Zhang, and A. Anselmo (1997), *Transport phenomena in Czochralski crystal growth process*, Advances in Heat Transfer, 30, pp. 313–435.
[30] F. Quirós and J. L. Vázquez (2000), *Asymptotic convergence of the Stefan problem to Hele-Shaw*, Trans. Amer. Math. Soc., 353, pp. 609–634.
[31] T. Sinno, E. Dornberg, W. von Ammon, R. A. Brown, and F. Dupret (2002), *Defect engineering of Czochralski single-crystal silicon*, Material Science and Engineering Reports, 28, pp. 149–198.
[32] V. A. Tatarchenko (1993), *Shaped Crystal Growth*, Kluwer Academic Publishers, Boston.
[33] K. Tanahasji, M. Kikuchi, T. Higashino, N. Inoue, and Y. Mizokawa (2000), *Concentration of point defects changed by thermal stress in growing CZ silicon crystal: Effect of the growth rate*, J. Crystal Growth, 210, pp. 45–48.
[34] J. Völkl (1994), *Stress in the cooling crystal*, in Handbook of Crystal Growth, Vol. 2B, D. T. J. Hurle, ed., North–Holland, Amsterdam, pp. 821–874.
[35] S. Weinbaum, and L. M. Jiji (1977), *Singular perturbation theory for melting or freezing in finite domains initially not at the fusion temperature*, J. Appl. Mech., 44, pp. 25–30.
[36] G. W. Young and A. Chait (1990), *Surface tension driven heat, mass, and momentum transport in a two-dimensional float-zone*, J. Crystal Growth, 106, pp. 445–466.
[37] G. W. Young and J. A. Heminger (1997), *Modeling the time-dependent growth of single-crystal fibers*, J. Crystal Growth, 178, pp. 410–421.
[38] G. W. Young and J. A. Heminger (2000), *A mathematical model of the edge-defined film-fed growth proccess*, J. Engrg. Math., 38, pp. 371–390.
[39] M. M. Yan and P. N. S. Huang (1979), *Perturbation solutions to phase change problem subject to convection and radiation*, J. Heat Transfer, 101, pp. 96–100.